Dating protracted fault activities: microstructures, microchemistry and geochronology of the Vaikrita Thrust, Main Central Thrust zone, Garhwal Himalaya, NW India

Chiara Montemagni[1*], Chiara Montomoli[2], Salvatore Iaccarino[3], Rodolfo Carosi[3], Arvind K. Jain[4], Hans-J. Massonne[5] & Igor M. Villa[1,6,7]

1 - Dipartimento di Scienze dell'Ambiente e della Terra, Università degli Studi di Milano Bicocca, Piazza della Scienza 4, 20126 Milano, Italy
2 - Dipartimento di Scienze della Terra, Università di Pisa, v. S. Maria 53, 56126 Pisa, Italy
3 - Dipartimento di Scienze della Terra, Università di Torino, v. Valperga Caluso 35, 10125, Torino, Italy
4 - CSIR-Central Building Research Institute, Roorkee -247667, Uttarakhand, India
5 - Institut für Mineralogie und Kristallchemie, Universität Stuttgart, Azenbergstraße 18, D-70049 Stuttgart, Germany
6 - Institut für Geologie, Universität Bern, Baltzerstrasse 3, 3012 Bern, Switzerland
7 - Centro Universitario Datazioni e Archeometria, Università degli Studi di Milano Bicocca, 20126 Milano, Italy

*Corresponding author (c.montemagni@campus.unimib.it)

Short Title

Geochronology of the Vaikrita Thrust

Abstract

The timing of shearing along the Vaikrita Thrust, the structurally upper boundary of the Main Central Thrust zone (MCTz), was constrained by combined microstructural, microchemical and geochronological investigations. Three different biotite-muscovite growth and recrystallisation episodes were observed: a relict mica-1; mica-2 along the main mylonitic foliation; mica-3 in coronitic structures around garnet during its breakdown.

Analyses of biotite by electron microprobe show chloritization, and bimodal composition of biotite-2 in one sample. Muscovite-2 and muscovite-3 differ in composition from each other.

Biotite and muscovite ^{39}Ar-^{40}Ar age spectra from all samples give both inter-sample and intra-sample discrepancies. Biotite step ages range between 8.6 and 16 Ma, muscovite step ages between 3.6 and 7.8 Ma. These ages cannot be interpreted as "cooling ages", as samples from the same outcrop cooled simultaneously. Instead, Ar systematics reflect sample-specific recrystallisation markers. Intergrown impurities were diagnosed by Ca/K ratios. Age data of biotite were interpreted as a mixture of true biotite-2 (9.00±0.10 Ma) and two alteration products. The negative Cl/K-age correlation identifies a Cl-poor muscovite-2 (>7 Ma) and a Cl-rich, post-deformational, coronitic muscovite-3 grown at ≤5.88±0.03 Ma. The Vaikrita Thrust was active at least from 9 to 6 Ma around 600 °C; its movement ceased by 6 Ma. Constraining the age and duration of movements in shear zones is one of the major objectives in the study of the evolution of collisional belts (Challandes *et al.* 2003; Di Vincenzo *et al.* 2004; Carosi *et al*. 2006, 2010, 2016; Iaccarino *et al*., 2015, 2017a; Beltrando *et al*. 2009; Rolland *et al.* 2009; Sanchez *et al.* 2011; Montomoli *et al.* 2013, 2015; Cottle *et al.* 2015, Kellett *et al*. 2016), such as the Himalaya (Fig. 1a).

One of the main unsolved problems in the Himalayan belt is the nature of the Main Central Thrust (MCT), a first-order tectonic discontinuity that runs all over the length of the belt. The MCT, which divides the Greater Himalayan Sequence (GHS) from the underlying Lesser Himalayan Sequence (LHS), is a top to the S/SW ductile to brittle shear zone, dipping to the north. As discussed by Searle *et al.* (2008), Martin (2016) and Mukhopadhyay *et al.* (2017), the definition of the MCT has changed since the first one by Heim & Gansser (1939). The current debate is especially related to the criteria to define (and, thus, to localise) the MCT. Therefore, several definitions of the MCT have been proposed (see Searle *et al.* 2008, and Martin 2016 for an updated review) such as (1) a structural-metamorphic one (Heim & Gansser 1939); (2) a metamorphic-rheological (Searle *et al.* 2008) and a purely rheological one (e.g. Gibson *et al.* 2016; Parsons *et al.* 2016); (3) a chronological one (e.g. Webb *et al.* 2013); and (4) a compositional one, assuming that the MCT is a high-strain reverse kinematic zone that separates distinguishable protoliths (e.g. Martin *et al*. 2005; Martin 2016). Moreover, the MCT records a protracted deformation, from ductile to brittle (Carosi *et al*. 2007, and references therein), and affects several different lithologies along strike. This further complicates the debate.

The above controversy led to the definition of two distinct thrusts in NW India (Valdiya 1980; Saklani *et al.* 1991; Ahmad *et al.* 2000) and in Nepal (Hashimoto *et al.* 1973; Arita 1983; DeCelles *et al.* 2000, Robinson *et al.* 2001; Robinson 2008). In different areas of the belt these two bounding thrusts have been named in different ways, although they seem to refer to the same structural setting. In the Garhwal Himalaya (NW India), the MCTz is well exposed: Valdiya (1980) and Ahmad *et al.* (2000) defined the Munsiari Thrust at the bottom and the Vaikrita Thrust at the top of the MCTz, whereas Saklani *et al.* (1991) defined the lower thrust as MCT2 in the Yamuna valley.

The activity time-span of the MCT in different areas of the belt was estimated using mutually contrasting methods or criteria. This span ranges from 23-20 to 15 Ma in different areas of the belt (see Godin *et al.* 2006 and Montomoli *et al.* 2015 for an updated review) down to c. 3 Ma reported in central Nepal (Catlos *et al.* 2001). In the Garhwal Himalaya, several authors proposed their preferred ages of the MCT activity based on different chronometers (K-Ar, Th-Pb and ^{39}Ar-^{40}Ar) and especially on different non-isotopic sample characterisations. Metcalfe (1993) obtained K-Ar ages on biotite and muscovite from the Bhagirathi valley, about 100 km W of our study area (Fig. 1a). Based on these data, this author proposed that the MCT was active between 14 and 5.7 Ma. Catlos *et al.* (2002) extended their previous work on Nepal to western Garhwal beneath the Vaikrita Thrust and asserted that the Th-Pb ages of monazite constrain the age of the entire activity of the MCT in the central and western Himalaya to c. 6 Ma. Célérier *et al.* (2009) reported c. 9 Ma obtained using ^{39}Ar-^{40}Ar on muscovite from samples in the middle portion of the MCTz near the village of Helang. Sen *et al.* (2015) obtained ^{40}Ar-^{39}Ar biotite ages of c. 10 Ma and interpreted them as “cooling ages”, which were correlated to the exhumation of the GHS caused by MCT thrusting at that time. In addition, muscovite ages of c. 6 Ma were related to a late stage deformation post-dating biotite cooling (Sen *et al.* 2015). However, questions concerning microstructural and chemical features in context with the protracted deformation have not been addressed by any of these conflicting studies.

As our observations of the deformation style of the MCTz in Garhwal strongly suggests a more complex history than that described in previous studies, we apply here an integrated structural-microchemical-geochronological approach (Vance *et al.* 2003) to provide a time frame for the different styles of activity of the Vaikrita thrust. The baseline for any interpretation is a detailed microstructural study (e.g. Rolland *et al.* 2009; Montomoli *et al.* 2013, 2015; Iaccarino *et al.*, 2015), which is required to clarify the aforementioned contrasting estimates, as such a study can distinguish between pre-, syn-, and post- kinematic minerals. This can and should be linked to dated minerals applying analytical techniques that allow the recognition of heterochemical phases and simultaneously provide their age (e.g. analyses of monazite by electron microprobe and of mica, amphibole and feldspar by ^{39}Ar-^{40}Ar mass spectrometry: Villa & Williams 2013; Villa & Hanchar 2017).

A recognition of heterochemical mineral replacements, and of mineral disequilibria in general, is necessary to take into account the metamorphic reactions and fluid circulation that led to partial resetting and/or growth of new mineral chronometers (Challandes *et al.* 2003, Sanchez *et al.* 2011). The ignorance of the occurrence of several mineral generations must lead (and has led) to inaccurate age estimates. To this end, we report ^{39}Ar-^{40}Ar stepwise heating results on biotite and white-mica separates from very closely spaced mylonitic micaschist samples taken near the Vaikrita Thrust, the structural top of the MCTz. A feature of ^{39}Ar-^{40}Ar dating, most useful for the present study, is its ability to characterise the analysed phases by means of the Cl/K and Ca/K ratios (Müller *et al*. 2002), and thus to diagnose the presence of heterochemical retrogression phases. This is especially valuable when attempting to date fault movements, as sheared minerals are almost always affected by re-crystallisation, dissolution/reprecipitation and alteration, and by resulting grain sizes of a few µm only (Berger *et al*. 2017). This extreme comminution strongly limits the utility of mineral separations, as it, perforce, does not allow us to produce a monomineralic separate and, thus, limits the use of *in-situ* analyses, the spatial resolution of which is often insufficient to obtain results for a single-generation mineral (Müller *et al*. 2002). The impossibility of obtaining monomineralic separates can be circumvented by a judicious use of correlation diagrams (Villa & Hanchar 2017).

Geological background of the Himalaya

The Himalayan orogen formed by the closure of the Tethyan Ocean and the subsequent collision between India and Asia plates. Even if the timing of terminal collision has been debated in literature (Najman *et al*. 2017 and references therein) the age of collision has been recently constrained by Najman *et al*. (2017) at 54 Ma, at least in the NW portion of the belt. The Himalayan mountain belt is composed of several tectono-metamorphic units bounded by regional scale reverse and normal shear zones (Fig. 1): the Main Frontal Thrust (MFT), the Main Boundary Thrust (MBT), the Main Central Thrust (MCT) and the South Tibetan Detachment System (STDS) (Le Fort 1975). From south to north, the tectonic units of the belt are:

1. The Sub-Himalaya is constituted by Miocene to Pleistocene sediments, derived from the erosion of the belt (Hodges 2000), and delimited at the bottom by the MFT, a tectonic lineament that divides this unit from the underlying undeformed sediments of the Ganga plain. At the top of the Sub-Himalaya, the MBT divides this unit from the upper Lesser Himalayan Sequence (LHS).
2. The LHS (Fig. 1) is made of low to medium grade marble, orthogneiss, quartzite and schist being Lower Proterozoic to Early Palaeozoic in age (Hodges 2000). The MCT, a wide, ductile to brittle, top-to-the south shear zone divides the LHS from the overlying Greater Himalayan Sequence (GHS).
3. The GHS (Fig. 1), representing the metamorphic core of the belt, consists of a sequence of medium- to high-grade Late Proterozoic to Cambrian metamorphic rocks such as gneiss, schist, migmatite, and calc-silicate rocks, which are intruded by Oligocene – Miocene leucogranites named Higher Himalayan Leucogranites (HHL, Visonà *et al*. 2012). The

thickness of the GHS is variable (from 2-3 km up to 30 km, Carosi *et al*. 2010, 2014; Montomoli *et al*. 2013). At least two main metamorphic events have been recognized in the GHS: a first Eocene – Oligocene event in the kyanite stability field, characterized by high pressure conditions, and a Miocene event of medium-low pressure conditions (Pognante & Benna 1993; Iaccarino *et al*. 2015 and references therein) in the sillimanite to cordierite stability field. The STDS, a system of normal, ductile to brittle top-to-the north shear zones and faults, divides the GHS from the upper Tethyan Sedimentary Sequence (TSS, Caby *et al*. 1983; Burchfiel *et al*., 1992; Carosi *et al*. 1998).

(4) The TSS (Fig. 1) comprises Palaeozoic to late Mesozoic low-grade metamorphic and undeformed rocks (Le Fort 1975). The metamorphic grade considerably increases towards the structurally lower portion of the TSS, close to the STDS, up to lower amphibolite facies conditions (Hodges 2000; Dunkl *et al*. 2011; Montomoli *et al*. 2017).

Geological framework of the Garhwal Himalaya

The study area is located in the Garhwal Himalaya (Uttarakhand, NW India), where a complete structural transect across the MCTz, located between the villages of Helang and Joshimath, has been investigated (Fig. 1a,b). The Munsiari and Vaikrita Thrusts, limiting the MCTz, are shown in Fig. 2a,b,c. The Berinag Formation crops out near Helang, in the southernmost portion of the transect, and belongs to the Lesser Himalayan Sequence (LHS) (Fig. 1b). This formation consists of schist, quartzite and carbonate rock affected by a greenschist-facies metamorphism. The main foliation strikes NW-SE and dips 30-35° to the NE (Fig. 1c, Jain *et al.* 2014).

The Munsiari Formation crops out within the MCTz (Fig. 1b), and consists of mylonitic quartzite (Fig. 2a), Precambrian mylonitic orthogneiss (Fig. 2b), garnet-bearing micaschist, and calc-silicate rock (Fig. 1b, Jain *et al.* 2014). The main foliation strikes from W-E to NW-SE and dips 45° from N to NE (Fig. 1d), whereas the main stretching lineation is oriented N20, 45 NE. The main kinematic indicators at the mesoscale (Jain *et al.* 2014) are S-C and S-C-C’ fabrics and asymmetrical boudins pointing to a top-to-the S/SW sense of shear (Jain *et al*. 2014). At the microscale, the main kinematic indicators such as S-C fabric, σ and δ porphyroclasts and mica fish confirm a top-to-the-SW sense of shear. At the microscale, the samples of the Vaikrita Thrust show the main foliation (S_m) that overprints an older foliation (S_{m-1}), which is only locally preserved. Garnet is enveloped by the main foliation, whereas staurolite porphyroblasts are syn-kinematic and contain an internal foliation (S_i) concordant with the external one. Grain Boundary Migration (GBM, Passchier & Trouw 2005) and minor-static recrystallisation represent the main deformation mechanisms in quartz. Kinematic indicators such as S-C-C’ fabric, mica fish and σ/δ-porphyroclasts indicate a top-to-SW sense of shear (Jain *et al.* 2014).

Spencer *et al.* (2012) identified the MCT “*sensu stricto*” with the Vaikrita Thrust (Fig. 2c), a ductile shear zone separating the lower Munsiari Formation from the upper Joshimath Formation belonging to the GHS. Thakur *et al.* (2015) defined the MCTz as a package of sheared rocks bounded by two discrete thrusts, namely the Munsiari Thrust at the bottom and the Vaikrita Thrust at the top, suggesting that the MCTz in the study area corresponds to the Lesser Himalayan Crystalline Sequence (LHCS, Virdi 1986) consisting of low- to medium-grade metamorphic rocks.

Spencer *et al.* (2012) and Thakur *et al.* (2015) estimated *P-T* conditions of the MCTz in the study area. The data of these authors agree within the given uncertainties. The former authors used “classical geothermobaric methods” (several cation exchange thermometry and net-transfer reactions barometry) and estimated peak *P-T* conditions between 0.5-1.1 GPa and 500-600° C. Thakur *et al.* (2015) estimated *P-T* conditions of 0.63-0.75 GPa and 550-582° C through pseudosection modeling and multi-equilibrium thermobarometry. Th-Pb monazite as young as c. 6 Ma were obtained by Catlos *et al.* (2002) near our study area in Garhwal. However, the age data are decoupled from petrological and textural context, and the overall interpretation remains ambiguous. Sen *et al.* (2015) reported ^{40}Ar-^{39}Ar ages on biotite of c. 10 Ma and on muscovite of c. 6 Ma for rocks from the Vaikrita Thrust.

The Joshimath Formation, which forms the lower portion of the GHS in the study area (Fig. 1b, 2d; Spencer *et al.* 2012; Thakur *et al.* 2015), consists of paragneiss, schist, and minor calc-silicate, in which the main foliation strikes from WNW-ESE to NW-SE and dips 35-40° from N to NE (Fig. 1e; Jain *et al.* 2014). At the microscale, rocks of the Joshimath Formation show the common mineral assemblage garnet, kyanite, quartz, muscovite, plagioclase, biotite and minor staurolite. According to Thakur et al. (2015), garnet porphyroblasts show inclusions of quartz, biotite and plagioclase.

Structurally upward, the Suraithota and Bhapkund Formations (Jain *et al.* 2014) represent the middle and upper GHS in the study area. According to Jain *et al*. (2014), the Suraithota Formation consists of kyanite-garnet-biotite-bearing gneiss, micaschist, quartzite and amphibolite intercalations. The main foliation strikes N120°-150° with a dip of 30°-40° toward NE (Jain *et al.* 2014). The Bhapkund Formation includes aluminosilicate-garnet-biotite migmatitic gneiss, tourmaline-rich leucogranitic lenses and dikes, and the Malari leucogranite, a small pluton with an age of c. 19 Ma (U-Pb on zircon, Sachan *et al.* 2010) outcropping at the northern margin of the Bhapkund Formation. According to Sachan *et al.* (2010), the Malari pluton is an undeformed body crosscutting the STDS, whereas Spencer *et al.* (2012), Jain *et al.* (2014), Thakur *et al.* (2015), Sen *et al.* (2015) and Iaccarino *et al.* (2017b) challenged this interpretation. We also found no field evidence that the Malari leucogranite actually crosscuts the STDS.

Petrography and microstructures of selected samples

Three samples of mylonitic micaschist have been selected from the Vaikrita Thrust close to the village of Tapoban (Fig. 1b, red stars). Sample GW13-29 was collected < 30 m downhill from sample GW13-28, following the road between Joshimath and Suraithota. Sample GW13-29B was taken from the same outcrop, less than 1 m away from GW13-29. All samples display a main schistosity, referred to as S_m, accompanied by variably identifiable rare pre-S_m relicts and/or post-S_m static mineral growth.

Sample GW13-28 is a garnet-staurolite-two mica-bearing impure quartzite that also contains tourmaline, ilmenite, monazite and abundant late chlorite, partially replacing biotite and garnet (Fig. 3b). The main foliation (S_m) is defined by the shape preferred orientation (SPO) of muscovite (muscovite-2), biotite (biotite-2) and ilmenite. This foliation can be classified as disjunctive schistosity characterized by a discrete transition to domains of quartz-rich microlithons. Static recrystallisation of biotite and muscovite can be also sporadically found. In the phyllosilicate-rich layers garnet porphyroclasts are enveloped by the main foliation (Fig. 3a), whereas in the quartz-rich granoblastic domains garnet shows a skeletal aspect. Staurolite appears along the main foliation suggesting a syn-kinematic growth (Fig. 3a). The main recrystallisation mechanism in quartz is GBM supported by sutured and amoeboid grain boundaries (Fig. 3c). However, static annealing of quartz is sometimes discernible by straight grain boundaries and triple points. Kinematic indicators at the microscale are represented by asymmetric recrystallisation tails of micas and asymmetric strain shadows around garnet porphyroclasts (Fig. 3a) and foliation fishes (Fig. 3d; Passchier & Trouw 2005), which show a top-to-the S/SW sense of shear.

Sample GW13-29 is a mylonitic micaschist (Fig. 3e,f) with the mineral assemblage quartz, biotite, muscovite, garnet, plagioclase and ilmenite. The S_m is an anastomosing disjunctive schistosity defined by SPO of biotite (biotite-2) and muscovite (muscovite-2). Locally, within the microlithons, micas (micas-1) oriented at high-angle with respect to the S_m mark an older foliation (S_{m-1}, Fig. 3f). Garnet is enveloped by the main foliation and often contains aligned inclusions of quartz, plagioclase, micas and allanitic epidote, defining an internal foliation (S_i) that is non-continuous with the external one (S_e, Fig. 3e). Thus, garnet could be classified as intertectonic porphyroblast. However, in some circumstances inclusions in garnet are not aligned. The mica-2 generation is followed structurally by a static growth of larger mica (mica-3) around garnet grains (Fig. 3e).

Additional sporadic mica-3 grains are found in the matrix: they are oriented in the same direction as mica-2 but are not comminuted and suggest later, static growth by a process resembling Ostwald ripening and pseudomorphism. Relict biotite-1 and muscovite-1 may be present but are difficult to identify, as ductile deformation was very intense and has reduced the grain size of mica grains and given them a shredded appearance. The latest generation consists of large micas (muscovite-3 and minor biotite-3) forming coronitic structures around garnet. These micas are characterised by the lack of internal deformation (undulose extinction or kinking) in contrast to mica oriented along S_m. Moreover, static recrystallisation of biotite and muscovite is evident as mica flakes cross-cut S_m. Main deformation mechanisms were GBM followed by minor static recrystallisation of quartz. Asymmetric recrystallisation tails of garnet porphyroclasts indicate a top-to-the-S/SW sense of shear.

Sample GW13-29B is a garnet-biotite-bearing mylonitic micaschist (Fig. 3g,h) also containing quartz, muscovite, plagioclase and minor chlorite. The S_m, defined by the SPO of biotite (biotite-2) and muscovite (muscovite-2), can be classified as disjunctive schistosity. The microstructure is characterised by the alternation of granoblastic quartzofeldspathic layers and lepidoblastic layers. The main foliation envelops intertectonic garnet that contains aligned quartz inclusions defining an internal foliation (S_i) discordant to the external one (Fig. 3g,h). Muscovite and biotite crystals (micas-3) show a coronitic texture around garnet porphyroclasts (Fig. 3h). These micas lack undulose extinction, kinking and internal deformation (Fig. 3h). These features are, instead, observed in micas-2 (Fig. 3g,h). Kinematic indicators such as δ-porphyroclasts and prevalent type 1 mica fishes (Passchier & Trouw 2005) show a top-to-SW shear sense.

Mineral chemistry of micas

Electron microprobe (EMP) analyses were carried out with a CAMECA SX100 hosted at the Institut für Mineralogie und Kristallchemie at Universität Stuttgart, equipped with five wavelength-dispersive spectrometers, using an accelerating voltage of 15 kV and a beam current of 10 nA. Details on the analytical protocol are reported in Massonne (2012). Selected analyses of the different structurally-located micas from the studied samples are given in Table 1. Their compositional variabilities are shown in Figures 4 and 5. Muscovite and biotite analyses were recalculated as atoms per formula unit (apfu) on the basis of 11 and 22 oxygens for muscovite and biotite, respectively. Figure 4 displays representative BSE images, in which the variation in X_{Mg} (i.e.,Mg/(Mg+Fe)) and Ti concentration between micas along the main foliation and coronitic micas is highlighted.

Muscovite

In all three samples, white mica shows a limited compositional variation around the muscovite-celadonite join with Si ranging between 3.05 and 3.17 apfu (Fig. 5a). Muscovite in sample GW13-28 is characterised by Al/Si ratios higher than in the other samples (Fig. 5a). The Ti concentration (Fig. 5b) in muscovite of sample GW13-28 is lower (0.007-0.023 apfu) and less scattered than in samples GW13-29 and GW13-29B. In GW13-29, muscovite-2 contains more Ti (0.030-0.043 apfu) compared to muscovite-3 (0.013-0.030 apfu, Figs. 4 and 5b). The same trend was observed in sample GW13-29B (Fig. 5b), where the Ti contents in muscovite-2 (0.023–0.036 apfu) are, however, only somewhat higher than in mica-3 (0.017-0.035 apfu).

The Na/(Na+K) ratio (Guidotti & Sassi 2002; Fig. 5c) of muscovite in sample GW13-28 is higher (c. 0.12-0.14) than in samples GW13-29 and GW13-29B (0.06-0.09), which display similar trends. Muscovite-2 and muscovite-3 from sample GW13-29 have a Na/(Na+K) ratio between 0.06-0.09 and 0.06-0.08, respectively. Muscovite-2 and muscovite-3 from sample GW13-29B display similar Na/(Na+K) ratios to those of sample GW13-29 (0.06-0.08: muscovite-2; 0.07-0.08: muscovite-3).

The X_{Mg} ratio is lower in muscovite-3 than in muscovite-2. In sample GW13-28 X_{Mg} ranges between 0.46 and 0.64. Muscovite-2 in sample GW13-29 shows X_{Mg} values between 0.44 and 0.50, whereas X_{Mg} of muscovite-3 is between 0.39 and 0.47. X_{Mg} in muscovite-2 and muscovite-3 of sample GW13-29B ranges between 0.44 and 0.52 and between 0.40 and 0.51, respectively.

Biotite

The mass fractions of the three biotite generations are even more lopsided than those of muscovite: biotite-1 and -3 are extremely rare. In sample GW13-28, only biotite-2 was analysed. It shows a remarkable chemical variation (Fig. 5d,e,f); in particular, its X_{Mg} is higher and its Ti mostly lower than that of GW13-29 and GW13-29B. Biotite-2 is fairly homogeneous in GW13-29, whereas it shows two distinct compositional clusters in GW13-29B (Fig. 5d,e,f, green triangles).

The $\mathrm{Al}^{\mathrm{IV}}$ contents of biotite in sample GW13-28 (Fig. 5d) are more variable (2.55-2.87 apfu, Fig. 5d) than in biotite-2 and -3 of sample GW13-29 (2.53-2.66 apfu). Biotite from sample GW13-29B forms two compositional clusters discernable in X_{Mg} (0.38-0.40: biotite-2, 0.32-0.34: biotite-3) and $\mathrm{Al}^{\mathrm{IV}}$ (2.57-2.60 apfu: biotite-2, 2.60-2.68 apfu: biotite-3) plots (Fig. 5d).

The Ti concentrations in biotite from sample GW13-28 range between 0.12 and 0.19 apfu, whereas biotite-2 and -3 from sample GW13-29 have higher Ti contents (0.33 -0.36 apfu, except few analyses, and 0.22-0.31 apfu, respectively, Fig. 5e). The Ti concentration of biotite-2 in GW13-29 is detectably higher than that of GW13-29B (Figs. 4 and 5e).

Biotite from sample GW13-29B forms two compositional clusters of biotite-2 discernable in X_{Mg} (0.33-0.34; 0.38-0.40) having the same Ti concentration (c. 0.25-0.29 apfu, Fig. 5e). The six spot analyses having high X_{Mg} all correspond to corroded grains, which might be interpreted as early schistosity-parallel biotite, whereas the other spot analyses with low X_{Mg} correspond to grains with straight grain boundaries.

Biotite in sample GW13-29B shows three compositional clusters (Fig. 5e). One corresponds to biotite-3, characterised by Ti contents between 0.18 and 0.30 and X_{Mg} of 0.33-0.35, identical to that of GW13-29. Two correspond to biotite-2, which shows a bimodal chemical composition: one with Ti concentrations between 0.26 and 0.29 apfu and X_{Mg} values of 0.37-0.40 (Fig. 5e) and the other with the same values of the Ti concentration but X_{Mg} values of 0.33-0.34 (Fig. 5e).

The K concentrations versus X_{Mg} are shown in Fig. 5f. In sample GW13-28 almost half of the spot analyses yielded low, sub-stoichiometric K (and correspondingly high $\mathrm{Al}^{\mathrm{IV}}$) in biotite. These systematic deviations from the other biotite analyses clearly pertain to (partially) altered grains, as supported by the matching element sums below 96 % for these analyses. Both indicators point to a partial replacement by chlorite or smectite and confirm that this sample contains more alteration phases than the others. Both biotite-2 and -3 from sample GW13-29 are characterised by X_{Mg} between 0.32 and 0.35 and K concentrations of 1.82-1.91 apfu.

Ti-in-biotite and Ti-in-muscovite geothermometry

Methods

Thermal conditions of mica (re-)crystallisation, in regard of the different textural positions described above, were constrained through empirical geothermometers based on the Ti concentration in micas increasing with increasing temperature (Henry *et al.* 2005 and references therein; Chambers & Kohn 2012; Wu & Chen 2015). Henry & Guidotti (2002) and Henry *et al.* (2005), based on an extensive natural biotite dataset from graphite and rutile/ilmenite bearing samples, reconstructed a Ti-saturation surface for biotite of the *P*-*T* range of 0.4-0.6 GPa and 480-800°C. Based on this saturation surface, they proposed a relationship of between *T* and X_{Mg} and the Ti concentration of biotite, with an associated systematic uncertainty of ±24 °C in the lower *T* range, approaching ±12 °C in the higher *T* calibration range.

We applied the Ti-in-biotite thermometer proposed by Henry *et al.* (2005). The pressure at which the Ti-in-biotite thermometer was originally calibrated (0.4-0.6 GPa, Henry & Guidotti 2002; Henry *et al.* 2005) is lower than that estimated for rocks that are structurally close to the present ones (0.82-0.88 GPa, Spencer *et al.* 2012; c. 0.73–0.86 GPa, Thakur *et al.* 2015). Therefore, a conservative systematic uncertainty of 50°C on the calculated absolute *T* should be taken into account (e.g. Mottram *et al.* 2014b).

The pressure-dependent Ti-in-muscovite thermometer was proposed by Wu & Chen (2015), who empirically calibrated this thermometer for the *P-T* range of 0.1-1.4 GPa and 450-800 °C for ilmenite- and aluminosilicate-satured metapelite. The quoted error of the Ti-in-muscovite thermometer, as suggested by Wu & Chen (2015), is ± 65 °C. We applied the Ti-in-muscovite thermometer, following the assumption of a corresponding equilibrium pressure of 0.8 GPa, in agreement with the *P* estimates previously reported (see above). Calculation at lower P (0.6 GPa) shows only a very minor (around 5 °C) decrease in the *T* estimates. An additional source of bias is the fact that the present rocks do not match the paragenesis used to calibrate the thermometer. Therefore, absolute temperature estimates may be inaccurate, but temperature differences between different mica generations of the same rock are probably accurate (Bucher & Grapes 2011). The Ti-in-biotite and Ti-in-muscovite geothermometers, as any geothermobarometric method (Spear 1993), are not without pitfalls (e.g. Chambers & Kohn 2012), such as, for instance, kinetic problems related to the distance of micas from a Ti source (Waters & Charnley 2002). Moreover, aluminosilicate, required for the Ti-in-muscovite thermometer, is lacking in our samples, even if other Al-rich phases such as garnet and staurolite are present as buffer, so that the Ti-in-muscovite temperature should be regarded as semi-quantitative.

Results

For muscovite-2, the temperatures obtained with the Ti-in-muscovite thermometer range between 394 and 561 °C, 550 and 626 °C, and 591 and 655 °C for sample GW13-28, GW13-29B, and GW13-29, respectively (Fig. S-1). These estimates are similar to, but higher than, those by Spencer *et al.* (2012) and Thakur *et al.* (2015). For samples GW13-28, GW13-29B and GW13-29, the average temperatures are 522±41 °C, 609±15 °C and 632±13 °C, respectively. Average temperatures obtained from muscovite-3 are 538±42 °C for sample GW13-29 and 571±43 °C for sample GW13-29B and, thus, systematically lower than *T* derived from muscovite-2.

The Ti-in-biotite geothermometer applied to biotite-2 gave average temperatures of 522±45 °C for sample GW13-28, 647±41 °C for sample GW13-29, and 627±8 °C for sample GW13-29B. The calculated *T* for biotite-3 is 631±18 °C and 607±27 °C for samples GW13-29 and GW13-29B, respectively, somewhat lower than for biotite-2. The obtained temperatures for both muscovite-2 and biotite-2 from sample GW13-28 are about 90-100 °C lower than for the other samples. This low temperature estimate parallels the compositional evidence for retrograde reactions (Fig. 5f) and suggests that the chloritization occurred during exhumation at lower *T* (cfr. also Massonne *et al.* 2017). In all samples, the calculated temperatures span a large range, which is compatible with a prolonged shearing and recrystallization history. Even taking into account the cautionary notes mentioned above, two factors strengthen our temperature estimates, which are sufficient for the interpretation of ^{39}Ar-^{40}Ar data: (1) the temperatures calculated using two different thermometers match within the corresponding uncertainties and (2) they are similar to the previously reported temperatures of 550-590 °C (Spencer *et al.* 2012; Thakur *et al.* 2015), which are based on the application of several geothermometric methods (e.g. garnet-biotite thermometer, Ti-in-biotite thermometer and multi-equilibrium thermobarometry) for samples in close proximity to the present ones. These temperature estimates are similar to those recorded by fluid inclusions in quartz near the Munsiari Thrust, 1 km downsection (Montemagni *et al.* 2016), namely 500-520 °C.

^{39}Ar-^{40}Ar dating

Analytical techniques

Mineral separation for samples GW13-28, GW13-29, GW13-29B was performed at the Institut für Geologie at Universität Bern. The rocks were crushed and sieved. Biotite and muscovite in the 150 - 350 µm fraction were enriched with gravimetric methods and subsequently purified by extensive hand picking. Density separation of biotite was comparatively straightforward, as biotite is heavier than most major minerals in these rocks. Therefore, most biotite grains in the crushed and sieved sample were included in the separate. On the contrary, muscovite was not efficiently separable by density, and hand-picking was necessary. Only the largest and cleanest-looking grains were chosen. This operator-dependent bias is known to potentially affect samples featuring multiple deformation stages (Villa *et al.* 2014, p. 812). It is therefore expected that the shredded muscovite-2 generation was selectively left out in favour of the nearly-euhedral static muscovite-3 generation.

Mica samples were irradiated in the McMaster University Research Reactor (Hamilton, Canada) carefully avoiding Cd shielding. ^{39}Ar-^{40}Ar step-heating analyses were carried out using a double-vacuum resistance furnace attached to a NuInstruments Noblesse™ rare gas mass spectrometer at Dipartimento di Scienze dell'Ambiente e della Terra, Università di Milano Bicocca. The analytical procedure of the ^{39}Ar-^{40}Ar step-heating technique is reported in Villa *et al.* (2000). The irradiation monitor was Fish Canyon sanidine with an assumed age of 28.172 Ma (Rivera *et al*. 2011); the decay constants are those by Steiger & Jäger (1977).

Results

The first and foremost observation is that all six age spectra (Figs. 6a, 7a) are internally discordant. Even disregarding the steps that clearly do not pertain to mica *sensu stricto* (a first cut off is the Ca/K ratio, which should be lower than 0.03 in micas) the step ages range between 8.6 and 16 Ma for biotite and 3.6 and 7.8 Ma for muscovite. These results are apparently similar to those reported by Sen *et al.* (2015) on nearby samples collected in the Suraithota Formation (Fig. 1a). Moreover, the age pattern featuring older biotite ages and younger muscovite ages is also found in other MCTz localities (Jain, unpublished results; Mottram *et al*. 2015). The latter authors disregarded the biotite ages as due to excess Ar. In contrast, our interpretation of the results exploits the context between microstructural, microchemical and geochronological data and will be presented in the following paragraph.

Discussion

The remarkable microstructural and chemical complexity of the minerals of the MCTz mylonitic schists requires restricting the following discussion to samples, for which we have established a detailed microstructural and petrogenetic context. It must be pointed out that recent studies (e.g. Berger *et al.* 2017, and references therein) provide conclusive observational evidence that shear-induced recrystallisation is rarely complete and results in extremely small heterochemical relict phases hosted in the recrystallised mineral matrix. In contrast to the interpretation by Sen *et al.* (2015), we will focus on the microstructures and argue that our results reflect a true diachronism. This is made possible by the fact that the selected three samples share the same geological history at the 10 m scale, but record different stages of the microstructural evolution. In the following, we will first focus on the similarities and the differences of the biotite results and then discuss the muscovite results, drawing attention to the observational and interpretive constraints provided by processes affecting biotite. Firstly, it is important to note that the biotite separates analysed here belong to an older mica generation than the muscovite separates. We further propose that discordant steps with low Ca/K and high step ages should be seen as inherited Ar of the sparse relicts of the biotite-1 generation. Therefore, there is no need to invoke excess Ar to explain why biotite-2 is older than muscovite-3. As inherited and excess Ar pertain to two completely different geochemical scenarios (Villa *et al.* 2014, p. 817), namely Ar loss and Ar gain, respectively, neglecting this difference would distort the entire interpretive framework.

The biotite age spectra are not only internally discordant (Fig. 6a) but also suggest different Ar retention over an extremely small distance. This indicates that "cooling" (Sen *et al.* 2015) is unlikely to be the only factor controlling the biotite ages. Because age spectra only provide an incomplete information (Chafe *et al.* 2014), it is necessary to also take into account the information provided by the (often neglected) isotopes ^{38}Ar and ^{37}Ar, which are produced from Cl and Ca in the reactor, respectively (Merrihue 1965). From the measured ^{38}Ar/^{39}Ar and ^{37}Ar/^{39}Ar ratios and the known production factors it is possible to calculate the Cl/K and Ca/K ratios, respectively (which can, but need not, be validated by EPM analyses: Villa et al. 2000). Figure 6b shows the Cl/K-Ca/K common-denominator correlation diagram (e.g. Villa & Williams 2013, and references therein). Data-points for all three samples define a very peculiar V-shaped trajectory: the first heating steps of all samples have high Ca/K and high Cl/K ratios, which monitor the degassing of calcium-rich alteration phases. At higher oven temperatures, typical of biotite *sensu stricto* degassing (c. 900 °C), Cl/K and Ca/K ratios reach a minimum and the high-temperature steps show an increase of the Ca/K ratio at constant Cl/K. This pattern applies to biotite from all three samples, but to different degrees. The only way to account for these observations is to hypothesize a three-phase mixture, whereby each sample consists of a different mass fraction of the three end-member phases.

Considering the steps most closely matching the Ca-free stoichiometry of biotite, i.e. those with Ca/K < 0.001, it becomes evident that in sample GW13-28 there are none, one in sample GW13-29B, and four in GW13-29. As the micas are fine-grained and intergrown with their retrogression products at a scale < 10 μm, even handpicking cannot achieve a monomineralic separate. In terms of chronological information from biotite, this unexpected observation can be used advantageously, as follows from Fig. 6c. The three biotite separates show a similar, albeit less clearly defined, V-shaped trajectory as in Fig. 6b. The interpretation in terms of a mixture of at least three phases is upheld: the alteration phase(s) having step ages up to 16 Ma and high Ca/K and Cl/K are most abundant in sample GW13-28. The extrapolation of the age-Ca/K trend gives an apparent age > 16 Ma. This apparent age is very likely to be geologically meaningless, because of several possible artefacts pertaining to the presence of an alteration phase, such as decoupling of ^{40}Ar and recoiled ^{39}Ar during degassing of fine biotite-chlorite intergrowths (Di Vincenzo *et al.* 2003). Clear evidence for massive chloritisation of biotite GW13-28 is provided by its bulk K concentration of 4.61 %, as calculated from the total ^{39}Ar concentration**.** This low value attests a clear chloritization of biotite in this separate. Even if the chronological information provided by GW13-28 is meaningless per se, it can provide two kinds of constraints. Firstly, the trend defined by the chloritized biotite exhibits a shallow slope in the Cl/K vs. Ca/K diagram. The observation of a different trend in biotite GW13-29B (higher Cl/K and low, biotite-like Ca/K) suggests the presence of a different biotite generation with a different composition. Permissive evidence for this supposed earlier biotite generation was reviewed above (Fig. 5d). The second type of constraint provided by chloritized biotite GW13-28 is that it can act as a useful end-member on the effect of alteration for the other two biotite separates, which are much less altered but not negligibly so. Indeed, in Fig. 6c the biotite separates GW13-29 and 29B follow the same pattern as in Fig. 6b, with one branch of the V-shaped trajectory pointing towards GW13-28. The four steps from GW13-29 (Fig. 6d) corresponding to the lowest Ca/K ratios, i.e. most closely approximating biotite stoichiometry, gave an isochron age of 9.07 ± 0.60 Ma (2 sigma uncertainty) with an atmospheric intercept. The atmospheric intercept allows us to consider the average age of these four steps as a legitimate "isochemical age" (Müller *et al*. 2002) of 9.00 ± 0.10 Ma. Strictly speaking, this is a cooling age, as the retention of Ar by biotite is complete only below c. 530 °C (Villa 2015). What is most important here is that biotite-2 formed several Ma earlier than muscovite-3.

In contrast to the biotite concentrates, all muscovite separates gave significantly younger ages, between c. 6 and 7 Ma. Age spectra are discordant (Fig. 7a). Muscovite from GW13-28 (the sample with the most altered biotite) shows the most disturbed spectrum with some step ages < 5 Ma, the high Cl/K of which clearly identifies them as the degassing of alteration phases (Fig. 7a). GW 13-29B with the best preserved biotite also shows the least discordant muscovite spectrum. Common regression of the data for muscovite from GW13-29 and -29B in a single Cl/K-age diagram, justified by their spatial proximity (< 1 m) and compositional similarity, reveals a negative correlation (Fig. 7b): a relatively Cl-rich mica with an age $\leq 5.88\pm0.03$ Ma, and a Cl-poor one, > 7 Ma old. As the microstructural observations distinguish between a fine-grained, shredded muscovite-2 along the main foliation and a coarse-grained, statically grown coronitic muscovite-3, it is very likely that hand-picking did enrich muscovite-3 compared to muscovite-2, but the respective mass fraction of the two generations in our separates are unknown. It is therefore possible that the end-member of the correlation trend seen in Fig. 7b is actually the c. 9 Ma old muscovite-2, if its mass fraction (estimated by mass balance) did not exceed 25 %.

An age difference between older biotite and younger muscovite in similar rocks was also observed by Mottram *et al.* (2015) in samples from the MCTz from Sikkim. These authors seem to accept that retention of Ar in muscovite is quite high even if an ambient temperature of 600 °C was maintained over several Ma, as already documented by Di Vincenzo *et al.* (2004), Allaz *et al.* (2011) and Villa *et al.* (2014, p. 817). However, the discussion in Mottram *et al.* (2015), purely based on the assumption of thermally activated Fick's Law diffusion, is internally contradictory, as it fails to explain why biotite is reproducibly older than muscovite, contrary to micas from terrains affected by a static, monometamorphic event (e.g. Allaz *et al.* 2011, and references therein). The exclusive focus on Ar diffusion under the assumption of a static system also forfeits the opportunity to examine microstructures and microchemistry, and correlate both with mica ages.

Regarding Ar retention in micas, Villa *et al*. (2014) observed complete, or nearly complete, Ar retention in 100 µm sized phengite in metamorphic terrains at T > 500 °C. Villa (2015) went on to interpolate the retention of Ar in static, monometamorphic biotite and derived a revised Ar “closure temperature” estimate of c. 530 °C, in good agreement with the scarce reliable experimental data (see Villa 2010, 2015). This Ar retentivity is at the lower end of the estimated temperature interval for our Garhwal samples. The implication is that biotite records ages which are not much younger than the metamorphic event at temperatures recorded by Ti-in-biotite and Ti-in-muscovite thermometers (see above). The 9.00 ± 0.10 Ma isochemical age therefore is a cooling age close to the growth of biotite-2 in sample GW13-29. *A fortiori* does the 6 Ma age, inferred from the muscovite correlation diagrams, reflect the static growth (especially considering the updated diffusivity data for muscovite: Villa *et al*. 2014) of muscovite-3 during the subsequent exhumation.

Selective sampling bias due to handpicking could account for the observation of Fig. 7b, in which an anticorrelation between two clusters is seen in the Cl/K versus age diagram: muscovite from sample GW13-28 is older and has lower Cl/K (blue dots), whereas younger muscovite from samples GW13-29 and GW13-29B has higher Cl/K (pink and green dots). Mixing relatively Cl-rich static muscovite-3 with Cl-poor muscovite-2 yields a good anticorrelation of age and Cl/K ratio; the age of the foliation-parallel muscovite-2 is higher or equal to the oldest step, in the present case 7.6 Ma. By extrapolating the correlation trend towards lower Cl/K values it is possible to infer a muscovite-2 age matching the biotite-2 age of 9 Ma by assuming $Cl/K = 5 \times 10^{-5}$ for muscovite-2. The age of static mica growth is underconstrained, and we can only argue that it was less or equal to the lowest step age of 5.88 ± 0.03 Ma showing the Ca/Cl/K signature of bona fide muscovite.

In summary (Fig. 8), syn-tectonic growth of micas-2, defining the main mylonitic foliation at c. 9 Ma, constrains the age of shearing along the Vaikrita Thrust. The formation of coronitic micas-3 at 5.88 Ma post-dates the deformation due to shearing (Fig. 8) and is related to the advection of K (enabling the growth of K-mica at the expense of garnet), mediated by fluids. The uncommon pattern whereby biotite ages are apparently older than muscovite ages is proposed here to be due to a combination of three causes: (1) the size bias between coronitic muscovite-3 and foliation-forming muscovite-2 caused an artificial enrichment of the larger muscovite-3 grains in the analysed separate; (2) the strong preponderance of muscovite-3 over biotite-3 in the coronites, ensuring that only sporadic large biotite-3 crystals were available for selective hand-picking; and (3) the strong preponderance of biotite-2 over the other biotite generations (biotite-1 and -3) ensuring that a biotite separate would almost exclusively consist of biotite-2.

The age of shearing along the two bounding faults of the GHS, namely the MCT and the STDS, can help to discriminate among tectonic models (see Montomoli *et al*. 2013 for a review). Some models require MCT and STDS to be contemporaneous: the *Channel Flow* model (Beaumont *et al*. 2001, 2004), the *Wedge Extrusion* model (Hodges *et al*. 1992; Grujic *et al*. 1996; Vannay & Grasemann 2001) and the *Wedge Insertion* model (Webb *et al*. 2007). Other models do not necessarily require contemporaneity: the *Critical Taper* model (Platt 1993; Kohn 2008) and the *In-sequence Shearing* model (Carosi *et al*. 2010; Montomoli *et al*. 2013, 2015). The present results argue against contemporaneity. Iaccarino *et al*. (2017b) constrained the ductile shearing along the STDS in the Garhwal region (further N along the same transect of the present study) to between c. 20 and 15 Ma by U-(Th)-Pb *in situ* geochronology on monazite occurring in a high-temperature mylonite. The Bura Buri leucogranite in W Nepal, c. 300 km east of the present area (23-25 Ma old: Carosi *et al*. 2013) intruded the TSS and thus provides a clear limit for the termination of the movement along the STDS; the Shivling leucogranite (c. 80 km west of the present area) could represent a similar time limit around 23 Ma (Searle *et al*. 1999, and references therein). In the Yadong region multiple leucogranite intrusions, dated at 23-16 Ma by Liu *et al*. (2017), sealed the STDS at ≥ 20 Ma, further supporting the orogen-wide diachroneity of the STDS and MCT.

Conclusions

1. The MCTz rocks in Garhwal record several well resolvable deformations. Microstructural observations show complex superposition of tectonic foliations, marked by successive mica growth and recrystallisation episodes. Microchemical analyses show both pervasive secondary alteration and primary heterogeneity of biotite. Muscovite is less altered and less clearly heterogeneous.
2. Three different generations of micas were observed: mica-1 in a relict foliation at high-angle with respect to the main mylonitic one (S_m); mica-2, oriented along S_m, is characterised by small flakes of both muscovite and biotite; mica-3, consisting of large crystals of muscovite and rare biotite, in coronitic structures around garnet porphyroclasts. Mica-3 lacks undulose extinction; its microstructure and chemical composition suggest formation during retrogression and garnet breakdown.
3. ^{39}Ar-^{40}Ar age spectra are discordant and show both inter- and intra-sample discrepancies, which cannot be interpreted as "cooling age" differences, as samples from the same outcrop cooled

simultaneously. Instead, Ar systematics reflects sample-specific markers of heterochemical recrystallisation. The isochron age of the Ca-poor steps of biotite separate GW13-29 (i.e. the age of biotite-2) is 9.07 ± 0.60 Ma, corresponding to a weighted isochemical average age of the steps pertaining to biotite *sensu stricto* of 9.00 ± 0.10 Ma. Muscovite shows a negative correlation between the Cl/K ratio and age as a result of a mixture of a relatively Cl-rich mica (muscovite-3), 5.88±0.03 Ma old, and a Cl-poor muscovite-2, > 7 Ma old. The extrapolation of the correlation trend to low Cl/K values allows us to suggest, but not to constrain, an end-member (muscovite-2) as old as c. 9 Ma.

4. Combining microstructural, microchemical and geochronological data, we propose the following evolution: syntectonic growth of mica-2 occurred along the main foliation at c. 9 Ma; the formation of coronitic muscovite at 5.88 Ma post-dated the deformation due to shearing along the Vaikrita Thrust; minor to pervasive alteration of muscovite occurred before, during and after coronite growth.

5. The shearing along the Vaikrita Thrust lasted until at least 9 Ma ago, i.e. continued for 6-7 Ma after the cessation of the movement along the STDS in the same study area.

Acknowledgments

We thank T. Theye (Universität Stuttgart) for his support during the EMP analyses and V. Barberini (Università degli Studi di Milano Bicocca) for her assistance during ^{40}Ar/^{39}Ar dating. This Research was supported by PRIN 2015EC9PJ5 (to C. Montomoli and R. Carosi). Two anonymous reviewers and Editor Santosh Kumar are warmly thanked for their comments and suggestions that greatly improved the manuscript.

References

AHMAD, T., HARRIS, N., BICKLE, M., CHAPMAN, H., BUNBORY, J. & PRINCE, C. 2000. Isotopic constraints on the structural relationship between the Lesser Himalayan Series and the High Himalayan Crystalline Series, Garhwal Himalaya. *Geological Society of America Bulletin,* **112**, 467-477.

ALLAZ, J., ENGI, M., BERGER, A. & VILLA, I. M. 2011. The effects of retrograde reactions and of diffusion on ^{40}Ar–^{39}Ar ages of micas. *Journal of Petrology*, **52(4)**, 691-716.

ARITA, K., 1983. Origin of the inverted metamorphism of the lower Himalaya, central Nepal. *Tectonophysics*, **95,** 43-60.

BEAUMONT, C., JAMIESON, R. A., NGUYEN, M. H., & LEE, B. 2001. Himalayan tectonics explained by extrusion of a low-viscosity crustal channel coupled to focused surface denudation. *Nature*, **414**, 738-742.

BEAUMONT, C., JAMIESON, R. A., NGUYEN, M. H., & MEDVEDEV, S. 2004. Crustal channel flows: 1. Numerical models with applications to the tectonics of the Himalayan□Tibetan orogen. *Journal of Geophysical Research: Solid Earth*, **109(B6)**.

BELTRANDO, M., LISTER, G. S., FORSTER, M., DUNLAP, W. J., FRASER, G., & HERMANN, J. 2009. Dating microstructures by the ^{40}Ar/^{39}Ar step-heating technique: deformation–pressure–temperature–time history of the Penninic units of the Western Alps. *Lithos*, **113(3)**, 801-819.

BERGER, A., WEHRENS, P., LANARI, P., ZWINGMANN H. & HERWEGH, M. 2017. Microstructures, mineral chemistry and geochronology of white micas along a retrograde evolution: An example from the Aar massif (Central Alps, Switzerland). *Tectonophysics*, **721**, 179–195.

BUCHER, K. & GRAPES, R. 2011. Petrogenesis of metamorphic rocks. *Springer Berlin Heidelberg.*

BURCHFIEL, B.C., CHEN, Z., HODGES, K.V., LIU, Y., ROYDEN, L.H., DENG, C., XU, J. 1992. The South Tibetan Detachment System, Himalayan Orogen. *Geological Society of America Special Paper*, **269** (41 pp.).

CABY, R., PÊCHER, A., LE FORT, P., 1983. Le grand chevauchement central himalayen:Nouvelles données sur le métamorphisme inverse à la base de la Dalle du Tibet. *Revue de Géologie Dynamique et de Géographie Physique*, **24**, 89–100.

CAROSI, R., GEMIGNANI, L., GODIN, L., IACCARINO, S., LARSON, K., MONTOMOLI, C., RAI, S. M. 2014. A geological journey through the deepest gorge on earth: The Kali Gandaki valley section, west-central Nepal. *Journal of the Virtual Explorer*, **47**, paper 7.

CAROSI, R., LOMBARDO, B., MOLLI, G., MUSUMECI, G., PERTUSATI, P.C. 1998. The south Tibetan detachment system in the Rongbuk valley, Everest Region. Deformation features and geological implication. *Journal of Asian Earth Sciences,* **16**, 299–311.

CAROSI, R., MONTOMOLI, C. & VISONÀ, D. 2002. Is there any detachment in the Lower Dolpo (Western Nepal)? *Comptes Rendus Geoscience*, **334**, 933–940.

CAROSI, R., MONTOMOLI, C. & VISONÀ, D. 2007. A structural transect in the Lower Dolpo: insights on the tectonic evolution of Western Nepal. *Journal of Asian Earth Sciences*, **29**, 407-423.

CAROSI, R., MONTOMOLI, C., IACCARINO, S., MASSONNE, H. -J., RUBATTO, D., LANGONE, A., GEMIGNANI, L. & VISONÀ, D. 2016. Middle to late Eocene exhumation of the Greater Himalayan Sequence in the Central Himalayas: Progressive accretion from the Indian plate. *Geological Society of America Bulletin*, **128(11-12)**, 1571-1592.

CAROSI, R., MONTOMOLI, C., RUBATTO, D. & VISONÀ, D. 2006. Normal-sense shear zones in the core of the Higher Himalayan Crystallines (Bhutan Himalaya): Evidence for extrusion?. *Geological Society, London, Special Publications*, **268**, 425-444.

CAROSI, R., MONTOMOLI, C., RUBATTO, D. VISONÀ, D. 2010. Late Oligocene high-temperature shear zones in the core of the Higher Himalayan Crystallines (Lower Dolpo, Western Nepal), *Tectonics*, **29**, TC4029, doi: 10.1029/2008TC002400.

CAROSI, R., MONTOMOLI, C., RUBATTO, D., & VISONÀ, D. 2013. Leucogranite intruding the South Tibetan Detachment in western Nepal: implications for exhumation models in the Himalayas. *Terra Nova*, **25(6)**, 478-489.

CATLOS, E. J., HARRISON, T. M., MANNING, C. E., GROVE, M., RAI, S. M., HUBBARD, M. S. & UPRETI, B. N. 2002. Records of the evolution of the Himalayan orogen from in situ Th–Pb microprobe dating of monazite: Eastern Nepal and western Garhwal. *Journal of Asian Earth Sciences*, **20**, 459-479.

CÉLÉRIER, J., HARRISON, T. M., BEYSSAC, O., HERMAN, F., DUNLAP, W. J. & WEBB, A. A. G. 2009. The Kumaun and Garwhal Lesser Himalaya, India; Part 2. Thermal and deformation histories. *Geological Society of America Bulletin*, **121**, 1281-1297.

CHAFE, A. N., VILLA, I. M., HANCHAR, J. M. & WIRTH, R. 2014. A re-examination of petrogenesis and ^{40}Ar/^{39}Ar systematics in the Chain of Ponds K-feldspar: "diffusion domain" archetype versus polyphase hygrochronology. *Contributions to Mineralogy and Petrology,* **167**, 1010, doi: 10.1007/s00410-014-1010-x.

CHALLANDES, N., MARQUER, D. & VILLA, I. M. 2003. Dating the evolution of C–S microstructures: a combined ^{40}Ar/^{39}Ar step-heating and UV laserprobe analysis of the Alpine Roffna shear zone. *Chemical Geology*, **197**, 3-19.

CHAMBERS, J. A. & KOHN, M. J. 2012. Titanium in muscovite, biotite, and hornblende: Modeling, thermometry, and rutile activities of metapelites and amphibolites. *American Mineralogist*, **97(4)**, 543-555.

COTTLE, J. M., SEARLE, M. P., JESSUP, M. J., CROWLEY, J. L. & LAW, R. D. 2015. Rongbuk re-visited: Geochronology of leucogranites in the footwall of the South Tibetan Detachment System, Everest Region, Southern Tibet. *Lithos*, 227, 94-106, doi: http://dx.doi.org/10.1016/j.lithos.2015.03.019.

DECELLES, P. G., GEHRELS, G. E., QUADE, J., LAREAU, B. & SPURLIN, M. 2000. Tectonic implications of U–Pb zircon ages of the Himalayan orogenic belt in Nepal. *Science*, **288**, 497-499.

DI VINCENZO, G., CAROSI, R. & PALMERI, R. 2004. The relationship between tectono-metamorphic evolution and argon isotope records in white mica: constraints from in situ ^{40}Ar–^{39}Ar laser analysis of the Variscan basement of Sardinia. *Journal of Petrology*, ***45***, 1013-1043.

DI VINCENZO, G., VITI, C., & ROCCHI, S. 2003. The effect of chlorite interlayering on 40Ar–39Ar biotite dating: an ^{40}Ar–^{39}Ar laser-probe and TEM investigations of variably chloritised biotites. *Contributions to Mineralogy and Petrology*, **145(6)**, 643-658.

DUNKL, I., ANTOLÍN, B., WEMMER, K., RANTITSCH, G., KIENAST, M., MONTOMOLI, C., DING, L., CAROSI, R., APPEL, E., EL BAY, R., XU, Q., & VON EYNATTEN, H. 2011. Metamorphic evolution of the Tethyan Himalayan flysch in SE Tibet. In: Growth and Collapse of the Tibetan Plateau. Eds. Gloaguen R., Ratschbacher L., *Geological Society of London Special Publications*, **353**: 45-69.

GIBSON, R., GODIN, L., KELLETT, D. A., COTTLE, J. M. & ARCHIBALD, D. 2016. Diachronous deformation along the base of the Himalayan metamorphic core, west-central Nepal. *Geological Society of America Bulletin*, **128**, 860-878.

GODIN, L., GRUJIC, D., LAW, R. D. & SEARLE, M. P. 2006.Channel flow, ductile extrusion and exhumation in continental collision zones: an introduction. *In*: Law, R. D., Searle, M. P. & Godin, L. (eds) *Channel Flow, Ductile Extrusion and Exhumation in Continental Collision Zones*. Geological Society, London, Special Publications, **268**, 1–23.

GRUJIC, D., CASEY, M., DAVIDSON, C., HOLLISTER, S.L., KÜNDIG, R., PAVLIS, T., & SCHMID, S. 1996. Ductile extrusion of the Higher Himalayan Crystalline in Bhutan: evidence from quartz microfabrics. *Tectonophysics*, **260**, 21–43.

GUIDOTTI, C.V. & SASSI F. P. 2002. Constraints on studies of metamorphic K-Na white micas. In: Micas: Crystal Chemistry & Metamorphic Petrology, *Reviews in Mineralogy and Geochemistry,* **46***,* 413-448.

HASHIMOTO, S., OHTA, Y. & AKIBA, C. lY73. Geology of the Nepal Himalayas. Saikon, Tokyo. 286 pp.

HEIM, A. A. & GANSSER, A. 1939. Central Himalaya: Geological observations of the Swiss Expedition, 1936. *Delhi, India, Hindustan Publishing*, pp. 26.

HENRY, D. J., & GUIDOTTI, C. V. 2002. Titanium in biotite from metapelitic rocks: Temperature effects, crystal-chemical controls, and petrologic applications. *American Mineralogist*, **87(4)**, 375-382.

HENRY, D. J., GUIDOTTI, C. V. & THOMSON, J. A. 2005. The Ti-saturation surface for low-to-medium pressure metapelitic biotites: Implications for geothermometry and Ti-substitution mechanisms. *American Mineralogist*, **90(2-3)**, 316-328.

HODGES, K.V. 2000. Tectonics of the Himalaya and southern Tibet from two perspectives. *Geological Society of America Bulletin*, **112**, 324-350.

HODGES, K.V., PARRISH, R.R., HOUSH, T.B., LUX, D.R., BURCHFIEL, B.C., ROYDEN, L.H., & CHEN, Z. 1992. Simultaneous Miocene extension and shortening in the Himalayan Orogen. *Science*, **258**, 1466–1470.

IACCARINO, S., MONTOMOLI, C., CAROSI, R., MASSONNE, H.-J. & VISONÀ, D. 2017a. Geology and tectono-metamorphic evolution of the Himalayan metamorphic core: insights from the Mugu Karnali transect, Western Nepal (Central Himalaya). *Journal of Metamorphic Geology*, **35**, 301-325, doi:10.1111/jmg.12233.

IACCARINO, S., MONTOMOLI, C., CAROSI, R., MASSONNE, H.-J., LANGONE, A. & VISONÀ, D. 2015. Pressure–temperature–time–deformation path of kyanite-bearing migmatitic paragneiss in the Kali Gandaki valley (Central Nepal): Investigation of Late Eocene–Early Oligocene melting processes. *Lithos,* **231**, 103-121.

IACCARINO, S., MONTOMOLI, C., CAROSI, R., MONTEMAGNI, C., MASSONNE, H.-J., LANGONE, A., JAIN, A.K., VISONÀ, D. 2017b. Pressure-Temperature-Deformation-Time constraints on the South Tibetan Detachment System in Garhwal Himalaya (NW India). *Tectonics,* **36**, 2281-2304, doi: 10.1002/2017TC004566.

JAIN, A. K., SHRESHTHA, M., SETH, P., KANYAL, L., CAROSI, R., MONTOMOLI, C., IACCARINO, S. & MUKHERJEE, P. K. 2014. The Higher Himalayan Crystallines, Alaknanda – Dhauli Ganga Valleys, Garhwal Himalaya, India. *In*: Montomoli, C., Carosi, R., Law, R., Singh, S. & Rai, S.M. (eds) *Geological field trips in the Himalaya, Karakoram and Tibet*. Journal of the Virtual Explorer Electronic Edition, **47**, paper 8.

KELLETT, D. A., WARREN, C., LARSON, K. P., ZWINGMANN, H., VAN STAAL, C. R., & ROGERS, N. (2016). Influence of deformation and fluids on Ar retention in white mica: Dating the Dover Fault, Newfoundland Appalachians. *Lithos*, **254**, 1-17.

KOHN, M. J. 2008. P□T□t data from Nepal support critical taper and repudiate large channel flow of the Greater Himalayan Sequence. *Geological Society of America Bulletin*, **120**, 259–273.

LE FORT, P. 1975. Himalayas: the collided range. Present knowledge of the continental arc. *American Journal of Science*, **275**, 1-44.

LIU, Z. C., WU, F. Y., QIU, Z. L., WANG, J. G., LIU, X. C., JI, W. Q., & LIU, C. Z. 2017. Leucogranite geochronological constraints on the termination of the South Tibetan Detachment in eastern Himalaya. *Tectonophysics (in press)*, doi:10.1016/j.tecto.2017.08.019.

MARTIN, A. J. 2016. A review of definitions of the Himalayan Main Central Thrust. *International Journal of Earth Science*, doi:10.1007/s00531-016-1419-8.

Martin, A. J., DeCelles, P. G., Gehrels, G. E., Patchett, P. J. & Isachsen, C. 2005. Isotopic and structural constraints on the location of the Main Central thrust in the Annapurna Range, central Nepal Himalaya. *Geological Society of America Bulletin,* **117**, 926-944.

Massonne, H.-J. 2012. Formation of amphibole and clinozoisite–epidote in eclogite owing to fluid infiltration during exhumation in a subduction channel. *Journal of Petrology*, **53(10)**, 1969-1998.

Massonne, H.-J., Cruciani, G., Franceschelli, M., & Musumeci, G. 2017. Anti-clockwise pressure-temperature paths record Variscan upper-plate exhumation: example from micaschists of the Porto Vecchio region, Corsica. *Journal of Metamorphic Geology*, doi: 10.1111/jmg.12283.

Merrihue, C. M. 1965. Trace-element determinations and potassium-argon dating by mass spectroscopy of neutron-irradiated samples. *Transactions of the American Geophysical Union*, **46**, 125.

Metcalfe, R. P. 1993. Pressure, temperature and time constraints on metamorphism across the Main Central Thrust zone and High Himalayan Slab in the Garhwal Himalaya. *Geological Society, London, Special Publications*, **74(1)**, 485-509.

Montemagni, C., Fulignati, P., Iaccarino, S., Marianelli, P., Montomoli, C. & Sbrana, A. 2016. Deformation and fluid flow in the Munsiari Thrust (NW India): a preliminary fluid inclusion study. *Atti Società Toscana Scienze Naturali*, **123**, 67-77, doi: 10.2424/ASTSN.M.2016.22.

Montomoli, C., Carosi, R. & Iaccarino, S. 2015. Tectonometamorphic discontinuities in the Greater Himalayan Sequence: a local or a regional feature? *In*: Mukherjee, S., van der Beek, P. & Mukherjee, P.K. (eds) *Tectonics of the Himalaya*. Geological Society, London, Special Publications, **412**, 21-41, doi: 10.1144/SP412.3.

Montomoli, C., Iaccarino, S., Antolin, B., Apple, E., Carosi, R., Dunkl, I., Ding, L., Visonà, D. 2017. Tectono-metamorphic evolution of the Tethyan Sedimentary Sequence (Himalayas, SE Tibet). *Italian Journal of Geosciences*, **136**: 73-88, doi: 10.3301/IJG.2015.42.

Montomoli, C., Iaccarino, S., Carosi, R., Langone, A. & Visonà, D. 2013. Tectonometamorphic discontinuities within the Greater Himalayan Sequence in Western Nepal (Central Himalaya): Insights on the exhumation of crystalline rocks. *Tectonophysics*, **608**, 1349-1370.

Mottram, C. M., Argles, T. W., Harris, N. B. W., Parrish, R. R., Horstwood, M. S. A., Warren, C. J. & Gupta, S. 2014a. Tectonic interleaving along the Main Central Thrust, Sikkim Himalaya. *Journal of the Geological Society,* **171**, 255–268.

Mottram, C. M., Parrish, R. R., Regis, D., Warren, C. J., Argles, T. W., Harris, N. B. & Roberts, N. M. 2015. Using U□Th□Pb petrochronology to determine rates of ductile thrusting: Time windows into the Main Central Thrust, Sikkim Himalaya. *Tectonics*, **34**, 1355-1374.

Mottram, C. M., Warren, C. J., Regis, D., Roberts, N. M., Harris, N. B., Argles, T. W. & Parrish, R. R. 2014b. Developing an inverted Barrovian sequence; insights from monazite petrochronology. *Earth and Planetary Science Letters*, **403**, 418-431.

Mukhopadhyay, D. K., Chakraborty, S., Trepmann, C., Rubatto, D., Anczkiewicz, R., Gaidies, F., Dasgupta, S. & Chowdhury, P. 2017. The nature and evolution of the Main Central Thrust: Structural and geochronological constraints from the Sikkim Himalaya, NE India. *Lithos*, doi:10.1016/j.lithos.2017.01.015.

Müller, W., Kelley, S. P. & Villa, I. M. 2002. Dating fault-generated pseudotachylytes: Comparison of ^{40}Ar/^{39}Ar stepwise-heating, laser-ablation and Rb-Sr microsampling analyses. *Contributions to Mineralogy and Petrology*, **144**, 57-77.

Najman, Y., Jenks, D., Godin, L., Boudagher-Fadel, M., Millar, I., Garzanti, E., Horstwood, M., & Bracciali, L. 2017. The Tethyan Himalayan detrital record shows that India–Asia terminal collision occurred by 54 Ma in the Western Himalaya. *Earth and Planetary Science Letters*, **459**, 301-310.

Parsons, A. J., Law, R. D., Lloyd, G. E., Phillips, R. J. & Searle, M. P. 2016. Thermo-kinematic evolution of the Annapurna-Dhaulagiri Himalaya, central Nepal: the Composite Orogenic System. *Geochemistry, Geophysics, Geosystems*, **17**, 1511-1539.

Passchier, C. W. & Trouw, R. A. J. 2005. Microtectonics. *Second Edition. Springer, Berlin.*

Platt, J. P. 1993. Exhumation of high-pressure rocks: a review of concept and processes. *Terra Nova*, **5**, 119–133.

Pognante, U. & Benna, P. 1993. Metamorphic zonation, migmatization and leucogranites along the Everest transect of eastern Nepal and Tibet: record of an exhumation history. *Geological Society, London, Special Publications*, **74(1)**, 323-340.

Rivera, T. A., Storey, M., Zeeden, C., Hilgen, F. J., & Kuiper, K. 2011. A refined astronomically calibrated ^{40}Ar/^{39}Ar age for Fish Canyon sanidine. *Earth and Planetary Science Letters*, **311(3)**, 420-426.

Robinson, D. M. 2008. Forward modeling the kinematic sequence of the central Himalayan thrust belt, western Nepal. *Geosphere*, **4**, 785-801.

Robinson, D. M., DeCelles, P. G., Garzione, C. N., Pearson, O. N., Harrison, T. M. & Catlos, E. J. 2001. The kinematic evolution of the Nepalese Himalaya interpreted from Nd isotopes. *Earth and Planetary Science Letters*, **192**, 507-521.

ROLLAND, Y., COX, S. F. & CORSINI, M. 2009. Constraining deformation stages in brittle–ductile shear zones from combined field mapping and ^{40}Ar/^{39}Ar dating: the structural evolution of the Grimsel Pass area (Aar Massif, Swiss Alps). *Journal of Structural Geology*, **31**, 1377-1394.

SACHAN, H. K., KOHN, M. J., SAXENA, A. & CORRIE, S. L. 2010. The Malari leucogranite, Garhwal Himalaya, northern India: chemistry, age, and tectonic implications. *Geological Society of America Bulletin*, **122**, 1865-1876.

SAKLANI, P. S., NAINWAL, D. C. & SINGH, V. K. 1991. Geometry of the composite Main Central Thrust (MCT) in the Yamuna Valley, Garhwal Himalaya, India. *Neues Jahrbuch für Geologie und Palaeontologie: Monatshefte*, **6**, 364-380.

SANCHEZ, G., ROLLAND, Y., SCHNEIDER, J., CORSINI, M., OLIOT, E., GONCALVES, P., VERATI, C., LARDEAUX, J. -M. & MARQUER, D. 2011. Dating low-temperature deformation by ^{40}Ar/^{39}Ar on white mica, insights from the Argentera-Mercantour Massif (SW Alps). *Lithos*, **125**, 521-536.

SEARLE, M. P., LAW, R. D., GODIN, L., LARSON, K. P., STREULE, M. J., COTTLE, J. M. & JESSUP, M. J. 2008. Defining the Himalayan Main Central Thrust in Nepal. *Journal of the Geological Society, London*, **165,** 523-534.

SEARLE, M. P., NOBLE, S. R., HURFORD, A. J., & REX, D. C. 1999. Age of crustal melting, emplacement and exhumation history of the Shivling leucogranite, Garhwal Himalaya. *Geological Magazine*, **136**, 513-525.

SEN, K., CHAUDHURYA, R. & PFÄNDER, J. 2015. ^{40}Ar–^{39}Ar age constraint on deformation and brittle–ductile transition of the Main Central Thrust and the South Tibetan Detachment zone from Dhauliganga valley, Garhwal Himalaya, India. *Journal of Geodynamics*, **88**, 1-13.

SPEAR, F. S. 1993. Metamorphic Phase Equilibria and Pressure- Temperature-Time Paths. Mineralogical Society of America, Washington, DC, 799 pp.

SPENCER, C. J., HARRIS, R. A. & DORAIS, M. J. 2012. The metamorphism and exhumation of the Himalayan metamorphic core, eastern Garhwal region, India. *Tectonics*, **31**, 1-18.

STEIGER, R., & JÄGER, E. 1977. Subcommission on geochronology: convention on the use of decay constants in geo-and cosmochronology. *Earth and planetary science letters*, **36**, 359-362.

THAKUR, S. S., PATEL, S. C. & SINGH, A. K. 2015. A P-T pseudosection modelling approach to understand metamorphic evolution of the Main Central Thrust Zone in the Alaknanda valley, NW Himalaya. *Contribution to Mineralogy and Petrology*, **170**, 1-26.

VALDIYA, K. S. 1980. The two intracrustal boundary thrusts of the Himalaya. *Tectonophysics*, **66**, 323-348.

VANCE, D., MÜLLER, W. & VILLA, I. M. (2003). Geochronology: linking the isotopic record with petrology and textures—an introduction. In: Vance, D., Müller, W. & Villa, I. M. (eds)

Geochronology: Linking the Isotopic Record with Petrology and Textures. Geological Society, London, Special Publications, **220**, 1-24.

VANNAY, J.C. & GRASEMANN, B. 2001. Himalayan inverted metamorphism and synconvergence extension as a consequence of a general shear extrusion. *Geological Magazine*, **138**, 253–276.

VILLA, I. M. & HANCHAR, J.M. 2017. Age discordance and mineralogy. *American Mineralogist,* doi: 10.2138/am-2017-6084.

VILLA, I. M. & WILLIAMS, M. L. 2013. Geochronology of metasomatic events. In: Harlov, D. E. & Austrheim, H. (eds) *Metasomatism and the Chemical Transformation of Rock*. Springer, Heidelberg, pp. 171–202.

VILLA, I. M. 2010. Disequilibrium textures versus equilibrium modelling: geochronology at the crossroads. *Geological Society, London, Special Publications*, **332**, 1-15.

VILLA, I. M. 2015. ^{39}Ar-^{40}Ar geochronology of mono-and polymetamorphic basement rocks. *Periodico di mineralogia*, **84**, 615-632.

VILLA, I. M., BUCHER, S., BOUSQUET, R., KLEINHANNS, I.C. & SCHMID, S.M. 2014. Dating polygenetic metamorphic assemblages along a transect across the Western Alps. *Journal of Petrology*, **55**, 803-830.

VILLA, I. M., HERMANN, J., MÜNTENER, O. & TROMMSDORFF, V. 2000. ^{39}Ar– ^{40}Ar dating of multiply zoned amphibole generations (Malenco, Italian Alps). *Contributions to Mineralogy and Petrology*, **140(3)**, 363-381.

VIRDI, N. S. 1986. Lithostratigraphy and structure of Central Crystallines in the Alaknanda and Dhauliganga valleys of Garhwal U.P. Himalayan thrusts and associated rocks. In: Saklani, P. S. (eds) *Current trends in geology*, **10**, 155–166.

VISONÀ, D., CAROSI, R., MONTOMOLI, C., PERUZZO, M. & TIEPOLO, L. 2012. Miocene andalusite leucogranite in central-east Himalaya (Everest–Masang Kang area): low-pressure melting during heating. *Lithos*, **144**, 194-208.

WATERS, D. J. & CHARNLEY, N. R. 2002. Local equilibrium in polymetamorphic gneiss and the titanium substitution in biotite. *American Mineralogist*, **87(4)**, 383-396.

WEBB, A. A. G., YIN, A., HARRISON, T. M., CÉLÉRIER, J. & BURGESS, W. P. 2007. The leading edge of the Greater Himalayan Crystalline complex revealed in the NW Indian Himalaya: implications for the evolution of the Himalayan orogen. *Geology*, **35**, 955-958.

WEBB, A. A. G., YIN, A. & DUBEY, C. S. 2013. U-Pb zircon geochronology of major lithologic units in the eastern Himalaya: implications for the origin and assembly of Himalayan rocks. *Geological Society of America Bulletin,* **125**, 499-522.

WEINBERG, R. F. 2016. Himalayan leucogranites and migmatites: nature, timing and duration of anatexis, *Journal of Metamorphic Geology,* **34***,* 821-843.

WU, C. M. & CHEN, H. X. 2015. Calibration of a Ti-in-muscovite geothermometer for ilmenite-and Al_2SiO_5-bearing metapelites. *Lithos*, **212**, 122-127.

Figure captions

Fig. 1: simplified geological map of (a) the Himalayas after Weinberg (2016) and (b) study area (after Jain *et al.* 2014). Red stars indicate the position of analysed samples. Sterographic projections (Wulff net, lower hemisphere) refer to main foliation measured in the different tectonic units: (c) the Lesser Himalayan Sequence, (d) the MCTz and (e) the Joshimath Formation from Jain *et al.* (2014).

Fig. 2: (a), (b) outcrops of the pervasively sheared rocks of the MCTz near the Munsiari Thrust, in which the kinematic indicators point a top-to-the-SW sense of shear (a) mylonitic impure marble with millimetric mica fish and asymmetrically deformed quartz porphyroclasts; (b) mylonitic orthogneiss with asymmetric tails around feldspar porphyroclasts; (c) outcrop of the Vaikrita Thrust with mylonitic micaschist interbedded with quartzitic levels showing top-to-the-SW sense of shear; (d) garnet-kyanite bearing paragneiss of the Joshimath Formation.

Fig. 3: microstructures of the Vaikrita Thrust. (a) garnet porphyroclast wrapped by the main foliation (S_m) , showing a top-to-the-SW sense of shear (sample GW13-28); (b) chloritization of biotite (sample GW13-28); (c) ameboid grain boundaries in quartz, testifying GBM recrystallization (sample GW13-28); (d) foliation fish pointing a top-to-SW sense of shear (GW13-28); (e) δ-type garnet porphyroclasts in sample GW13-29 showing a top-to-SW shear sense. Note the coronitic micas-3 around garnet; (f) S_m and relict S_{m-1} in mylonitic micaschist (sample GW13-29); (g) δ-type garnet porphyroclast, displaying a top-to-SW sense of shear, (sample GW13-29B); (h) detail of the inset in Fig. 3g. Note non-deformed coronitic micas and deformed micas on the S_m, intertectonic garnet shows a S_i discordant with respect to the S_m (sample GW13-29B). Mineral abbreviations: Bt – biotite, Grt – garnet, Qz– quartz, St – staurolite, Tur – torumaline, Ms - muscovite.

Fig. 4: representative BSE images with X_{Mg} value (bold) and Ti apfu concentration (italic) in white for muscovite and in yellow for biotite. (a), (b): sample GW13-28; (c), (d): sample GW13-29; (e),

Fig. 4: (a) ^{39}Ar-^{40}Ar age spectra of biotite comparing the three samples of the Vaikrita Thrust; (b) V-shaped trajectory of Cl/K vs Ca/K diagram. In the black box are highlighted the reliable low Ca – low Cl analyses, the dashed lines represent two trends: low Cl – variable Ca of the alteration phases of sample GW13-28 and variable Cl – low Ca trend; (c) age vs Cl/K correlation diagram of sample GW13-29 and GW13-29B. The dotted line contains the reliable analyses; (d) isochron obtained with the best four steps of sample GW13-29, corresponding to analyses contained in the dotted circle in (c).

Fig. 5: (a) ^{39}Ar-^{40}Ar age spectra of muscovite comparing the three samples of the Vaikrita Thrust. (b) Age vs Cl/K correlation diagram reveals a negative correlation between a Cl-rich mica, representing the coronitic white mica, and a Cl-poor one, possibly representing white mica along the S_p. Musc-2 – white mica along the Sp; Musc-3 – coronitic white mica around garnet.

Fig. S-1: histograms reporting thermometric data obtained with Ti-in-biotite and Ti-in-muscovite geothermometers. (a) and (c): data on white mica along the S_p (white mica-2) and coronitic around garnet (white mica-3), respectively; (b) and (d) data on biotite along the S_p (biotite-2) and coronitic around garnet (biotite-3), respectively. The legend in (b-d) is the same in (a).

Table captions

Table 1: representative electron microprobe analyses of white mica and biotite

Supplementary Table 1: ^{39}Ar-^{40}Ar data

Table 1

	Sample 28						**Sample 29**								**Sample 29B**							
	Muscovite			Biotite			Muscovite				Biotite				Muscovite				Biotite			
	Sp	Sp	Sp	Sp	Sp	Sp	cor.	cor.	Sp	Sp	cor.	cor.	Sp	Sp	cor.	cor.	Sp	Sp	cor.	cor.	Sp	Sp
SiO_2	46.14	46.27	46.00	34.36	34.98	33.54	45.37	46.09	45.79	45.64	34.28	34.28	34.60	34.50	44.98	46.17	45.62	45.13	33.99	34.31	34.13	35.00
TiO_2	0.44	0.45	0.39	1.52	1.27	1.55	0.49	0.29	0.77	0.79	2.48	2.36	3.07	3.04	0.33	0.47	0.72	0.68	1.56	1.86	2.33	2.52
Al_2O_3	33.79	34.06	33.85	18.82	18.93	19.16	33.46	33.93	32.42	32.41	17.27	17.15	17.24	16.90	33.98	34.26	33.08	32.77	18.16	17.47	17.40	17.91
FeO_{tot}	1.41	1.01	1.12	21.69	20.86	21.14	2.04	1.91	2.26	2.22	23.15	23.22	23.23	23.07	1.97	1.99	2.19	2.19	24.39	24.47	24.13	22.19
MnO	b.d.	b.d.	b.d.	0.05	0.04	0.01	b.d.	0.01	b.d.	b.d.	0.16	0.15	0.18	0.12	0.01	b.d.	0.01	b.d.	0.07	0.01	0.07	b.d.
MgO	1.06	0.91	1.00	8.82	8.64	9.78	0.83	0.89	1.18	1.08	6.67	6.86	6.87	6.84	0.77	0.91	1.05	1.04	7.22	7.11	6.90	8.04
CaO	b.d.	b.d.	0.01	b.d.	0.03	0.03	b.d.	0.01	b.d.	b.d.	0.01	0.01	b.d.	b.d.	0.02	b.d.	b.d.	b.d.	b.d.	0.01	b.d.	b.d.
BaO	0.19	0.13	0.19	0.11	0.05	0.06	0.30	0.27	0.31	0.31	0.15	0.13	0.15	0.25	0.24	0.24	0.21	0.21	0.10	0.13	0.18	0.20
Na_2O	0.90	0.92	0.91	0.07	0.28	0.06	0.59	0.65	0.54	0.56	0.13	0.08	0.16	0.15	0.58	0.62	0.62	0.49	0.09	0.09	0.07	0.08
K_2O	10.21	9.68	10.01	8.96	9.38	7.59	10.92	10.66	10.97	10.39	9.44	9.58	9.27	9.61	10.90	10.88	10.82	10.71	9.41	9.74	9.72	9.74
F	b.d.	0.05	0.09	0.29	0.38	0.18	0.05	b.d.	0.17	0.05	0.21	0.25	0.13	0.15	b.d.	b.d.	b.d.	0.08	0.28	0.04	0.19	0.24
Cl	b.d.	0.01	b.d.	0.04	0.12	0.04	b.d.	b.d.	b.d.	b.d.	0.03	0.02	0.02	0.02	0.01	b.d.	b.d.	0.01	0.03	0.03	0.02	0.03
Tot	94.15	93.49	93.58	94.73	94.94	93.13	94.05	94.70	94.42	93.44	93.96	94.08	94.92	94.65	93.79	95.53	94.31	93.32	95.30	95.25	95.15	95.96
Si	3.12	3.13	3.12	5.33	5.39	5.24	3.09	3.11	3.12	3.13	5.43	5.43	5.42	5.43	3.07	3.09	3.10	3.10	5.33	5.40	5.37	5.39
Ti	0.02	0.02	0.02	0.18	0.15	0.18	0.03	0.01	0.04	0.04	0.30	0.28	0.36	0.36	0.02	0.02	0.04	0.04	0.18	0.22	0.28	0.29
Al	2.69	2.71	2.70	3.44	3.44	3.53	2.69	2.70	2.60	2.62	3.23	3.20	3.18	3.14	2.74	2.70	2.65	2.65	3.36	3.24	3.23	3.25
Fe	0.08	0.06	0.06	2.81	2.69	2.76	0.12	0.11	0.13	0.13	3.07	3.08	3.04	3.04	0.11	0.11	0.12	0.13	3.20	3.22	3.18	2.86
Mn	--	--	--	0.01	0.00	0.00	--	0.00	--	--	0.02	0.02	0.02	0.02	0.00	--	0.00	--	0.01	0.00	0.01	--
Mg	0.11	0.09	0.10	2.04	1.98	2.28	0.08	0.09	0.12	0.11	1.57	1.62	1.60	1.61	0.08	0.09	0.11	0.11	1.69	1.67	1.62	1.85
Ca	--	--	0.00	--	0.00	0.01	--	0.00	--	--	0.00	0.00	--	--	0.00	--	--	--	--	0.00	--	--
Ba	0.00	0.00	0.01	0.01	0.00	0.00	0.01	0.01	0.01	0.01	0.01	0.01	0.01	0.02	0.01	0.01	0.01	0.01	0.01	0.01	0.01	0.01
Na	0.12	0.12	0.12	0.02	0.08	0.02	0.08	0.08	0.07	0.07	0.04	0.02	0.05	0.05	0.08	0.08	0.08	0.07	0.03	0.03	0.02	0.02
K	0.88	0.83	0.87	1.77	1.84	1.51	0.95	0.92	0.95	0.91	1.91	1.94	1.85	1.93	0.95	0.93	0.94	0.94	1.88	1.95	1.95	1.91
F	--	0.01	0.02	0.14	0.19	0.09	0.01	--	0.04	0.01	0.10	0.13	0.06	0.08	--	--	--	0.02	0.14	0.02	0.10	0.12
Cl	--	0.00	--	0.01	0.03	0.01	--	--	--	--	0.01	0.01	0.01	0.01	0.00	--	--	0.00	0.01	0.01	0.01	0.01
Tot	7.02	6.98	7.01	15.75	15.81	15.63	7.06	7.03	7.07	7.02	15.69	15.73	15.61	15.67	7.05	7.04	7.05	7.05	15.83	15.77	15.77	15.72

Atoms per formula unit are based on 11 oxygens for white mica and 22 for biotite. Abbreviation: Sp - micas on the main foliation; cor - coronitic micas around garnet; b.d. – below detection limit.

Figure 1

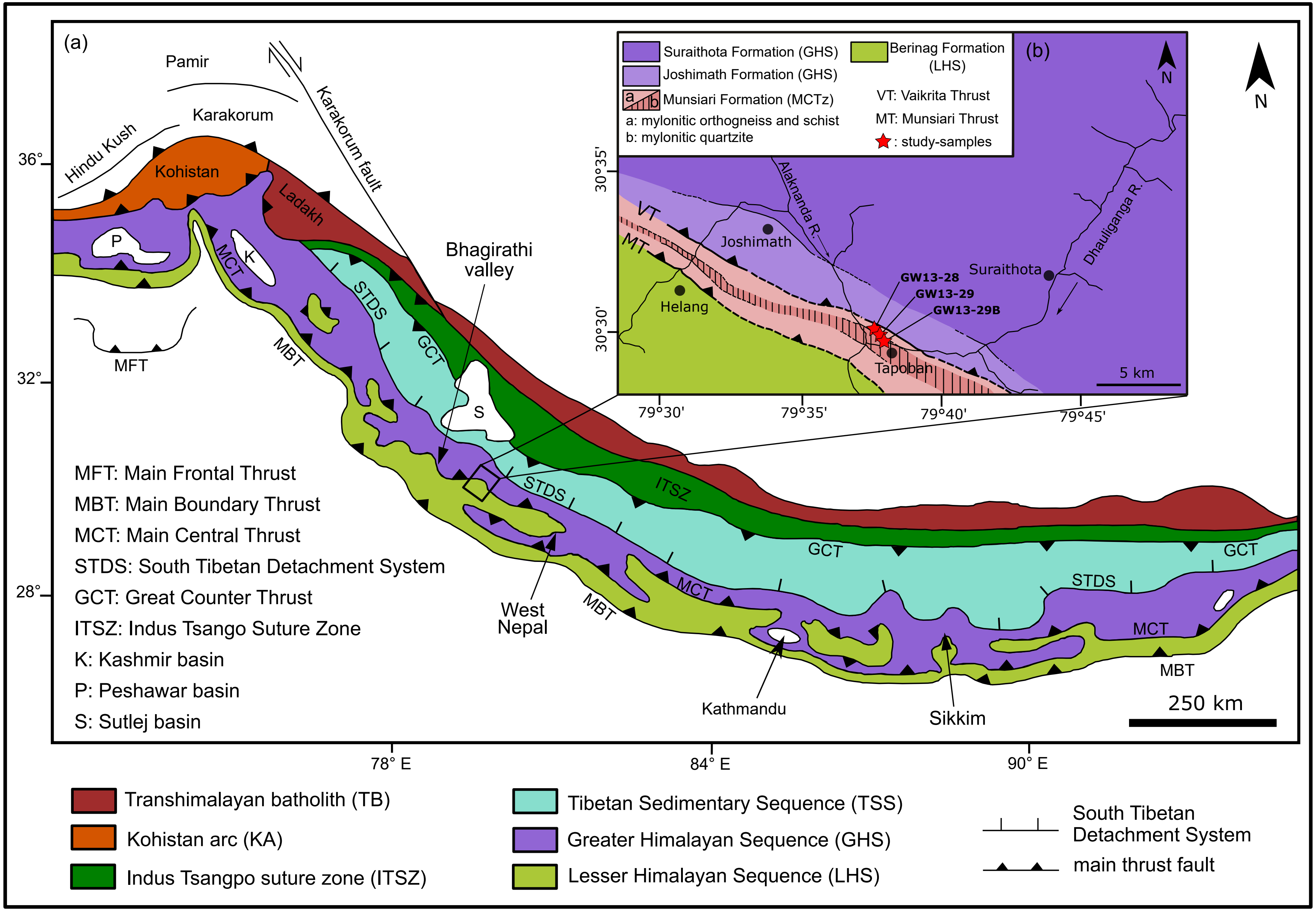
(a)
Pamir
Karakorum
Hindu Kush
Kohistan
Karakorum fault
Ladakh
P
K
MCT
MFT
MBT
STDS
GCT
S
Bhagirathi valley
ITSZ
STDS
GCT
MCT
MBT
West Nepal
Kathmandu
Sikkim
GCT
STDS
MCT
MBT
N
250 km
36°
32°
28°
78° E
84° E
90° E
MFT: Main Frontal Thrust
MBT: Main Boundary Thrust
MCT: Main Central Thrust
STDS: South Tibetan Detachment System
GCT: Great Counter Thrust
ITSZ: Indus Tsango Suture Zone
K: Kashmir basin
P: Peshawar basin
S: Sutlej basin
(b)
Suraithota Formation (GHS)
Joshimath Formation (GHS)
Munsiari Formation (MCTz)
a b
a: mylonitic orthogneiss and schist
b: mylonitic quartzite
Berinag Formation (LHS)
VT: Vaikrita Thrust
MT: Munsiari Thrust
: study-samples
N
VT
MT
Alaknanda R.
Dhauliganga R.
Joshimath
Helang
Suraithota
Tapoban
GW13-28
GW13-29
GW13-29B
5 km
30°35'
30°30'
79°30'
79°35'
79°40'
79°45'
Transhimalayan batholith (TB)
Kohistan arc (KA)
Indus Tsangpo suture zone (ITSZ)
Tibetan Sedimentary Sequence (TSS)
Greater Himalayan Sequence (GHS)
Lesser Himalayan Sequence (LHS)
South Tibetan Detachment System
main thrust fault

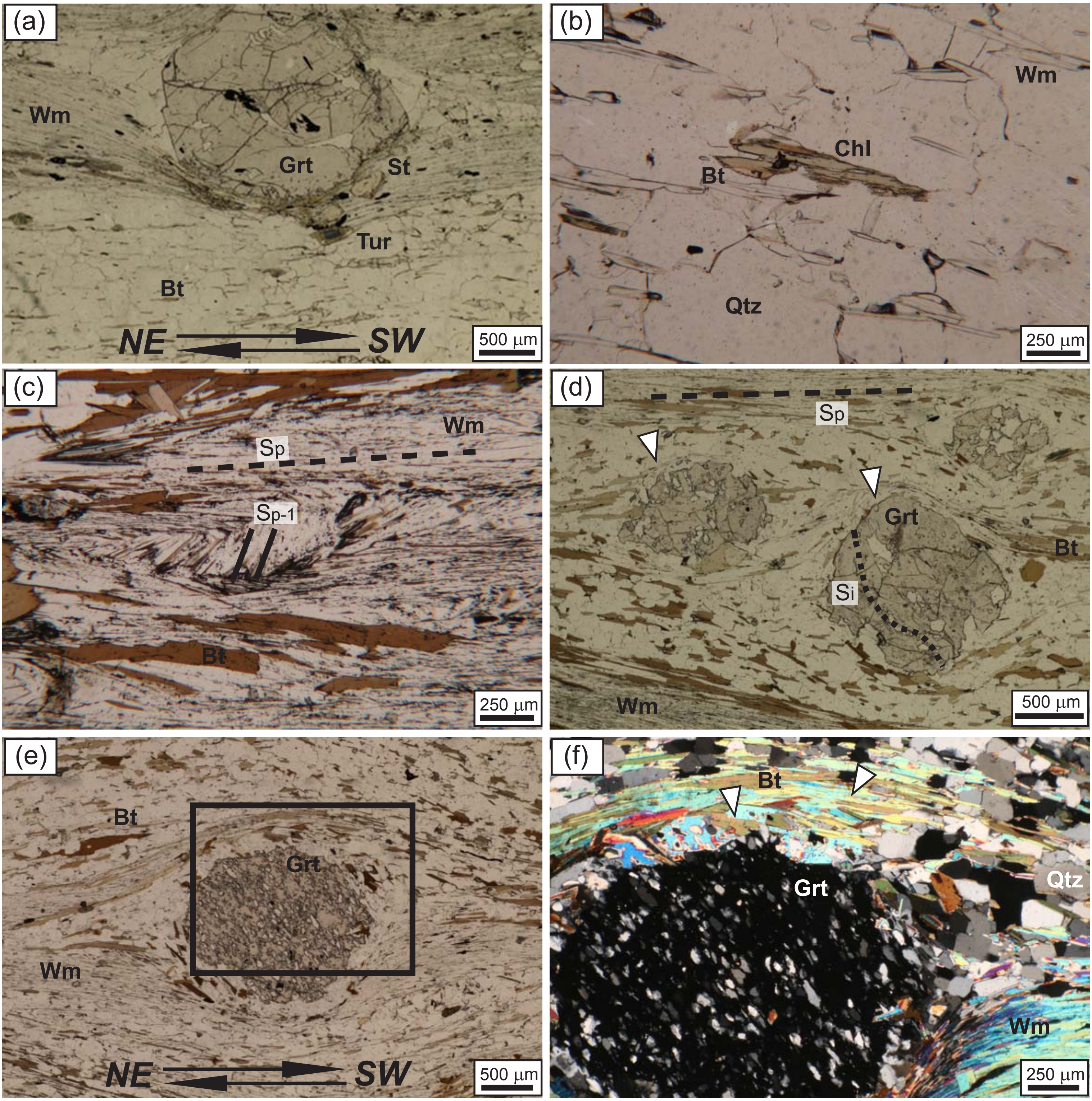
(a)
Wm
Grt
St
Tur
Bt
NE
SW
500 µm
(b)
Wm
Chl
Bt
Qtz
250 µm
(c)
Wm
Sp
Sp-1
Bt
250 µm
(d)
Sp
Grt
Bt
Si
Wm
500 µm
(e)
Bt
Grt
Wm
NE
SW
500 µm
(f)
Bt
Grt
Qtz
Wm
250 µm

Figure 3

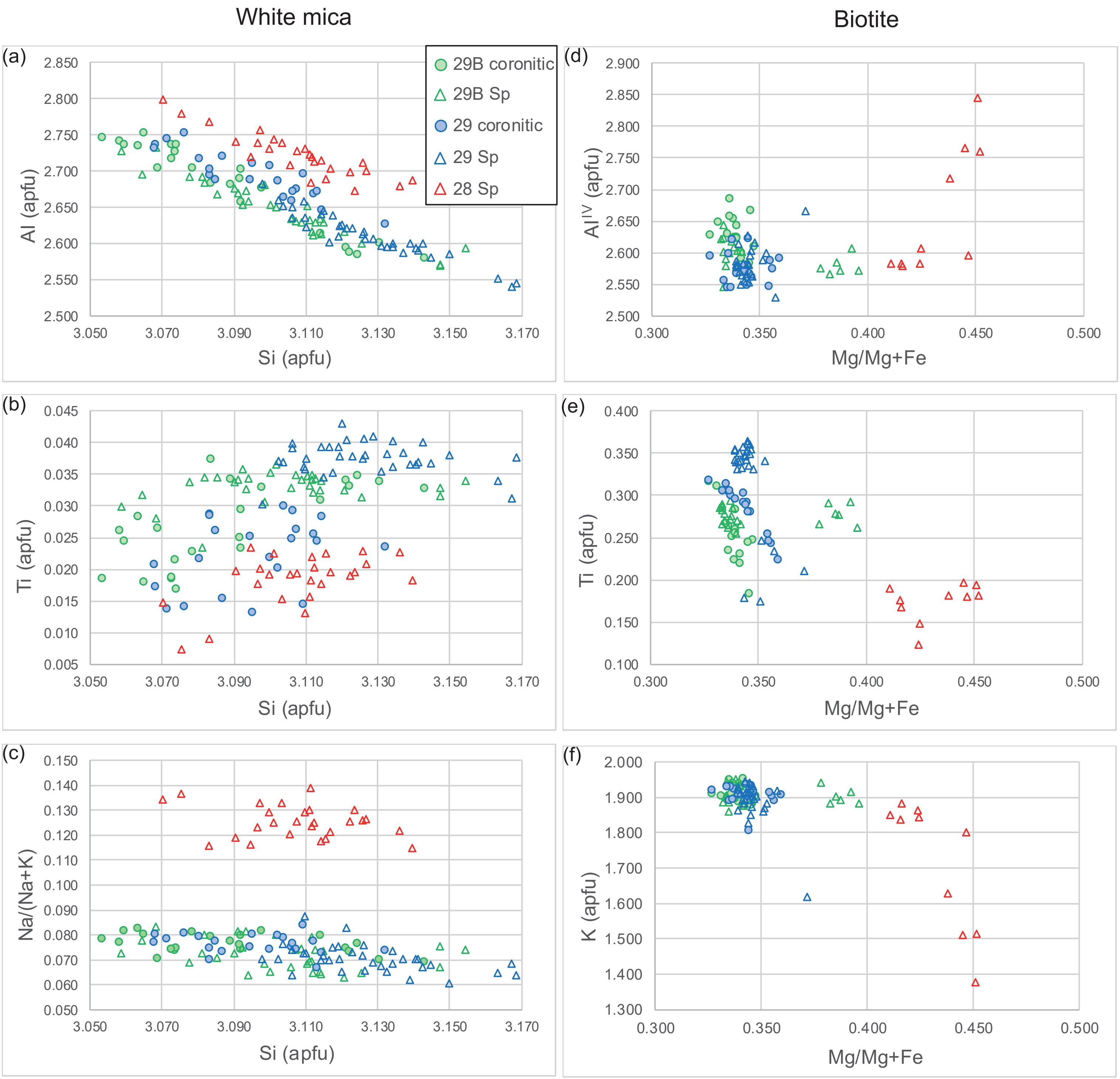
White mica
Biotite
(a)
Al (apfu)
2.850
2.800
2.750
2.700
2.650
2.600
2.550
2.500
3.050
3.070
3.090
3.110
3.130
3.150
3.170
Si (apfu)
● 29B coronitic
△ 29B Sp
● 29 coronitic
△ 29 Sp
△ 28 Sp
(d)
Al^{IV} (apfu)
2.900
2.850
2.800
2.750
2.700
2.650
2.600
2.550
2.500
0.300
0.350
0.400
0.450
0.500
Mg/Mg+Fe
(b)
Ti (apfu)
0.045
0.040
0.035
0.030
0.025
0.020
0.015
0.010
0.005
3.050
3.070
3.090
3.110
3.130
3.150
3.170
Si (apfu)
(e)
Ti (apfu)
0.400
0.350
0.300
0.250
0.200
0.150
0.100
0.300
0.350
0.400
0.450
0.500
Mg/Mg+Fe
(c)
Na/(Na+K)
0.150
0.140
0.130
0.120
0.110
0.100
0.090
0.080
0.070
0.060
0.050
3.050
3.070
3.090
3.110
3.130
3.150
3.170
Si (apfu)
(f)
K (apfu)
2.000
1.900
1.800
1.700
1.600
1.500
1.400
1.300
0.300
0.350
0.400
0.450
0.500
Mg/Mg+Fe

Figure 4

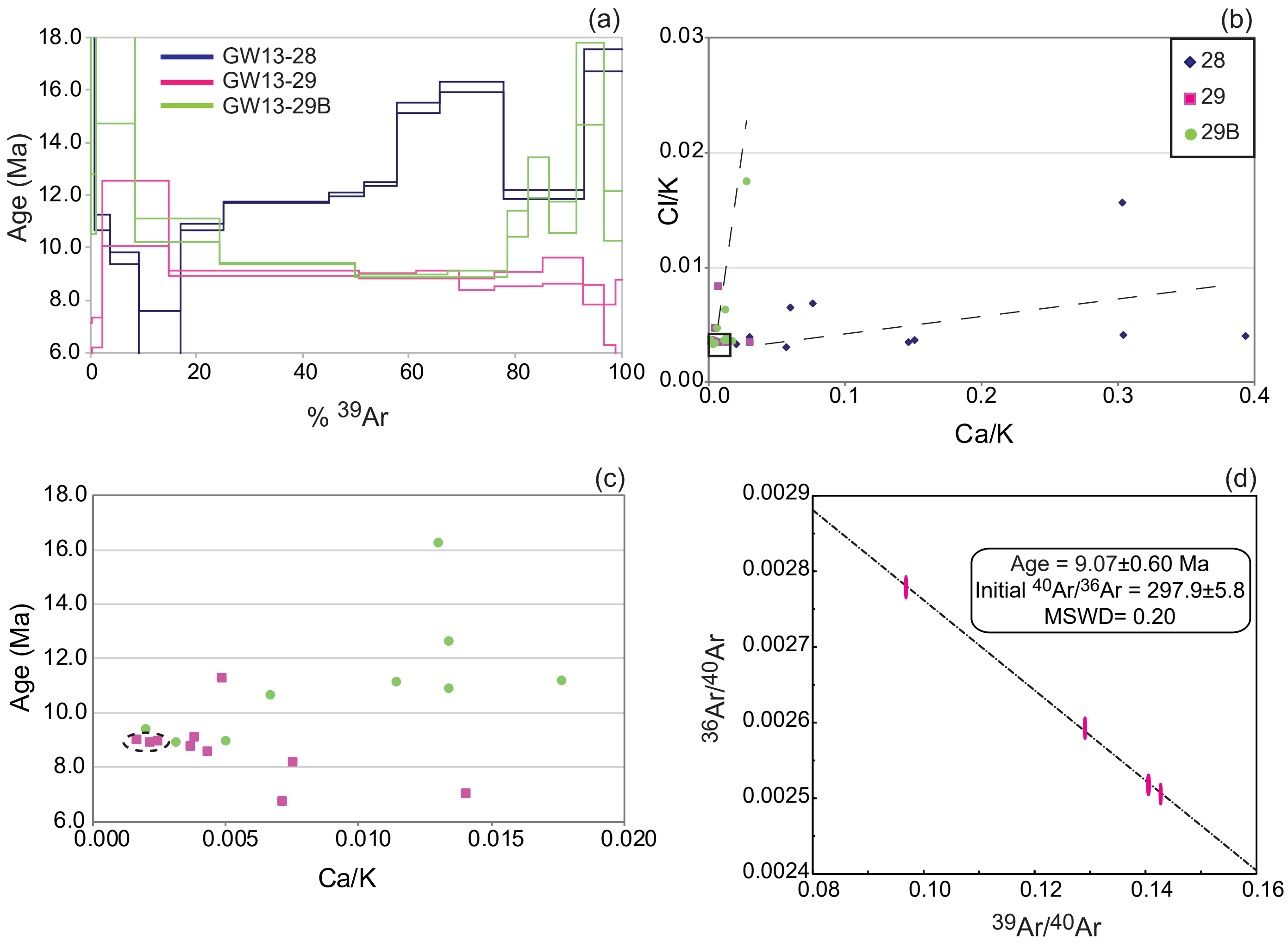
(a)
Age (Ma)
18.0
16.0
14.0
12.0
10.0
8.0
6.0
0
20
40
60
80
100
% 39Ar
GW13-28
GW13-29
GW13-29B
(b)
Cl/K
0.03
0.02
0.01
0.00
0.0
0.1
0.2
0.3
0.4
Ca/K
28
29
29B
(c)
Age (Ma)
18.0
16.0
14.0
12.0
10.0
8.0
6.0
0.000
0.005
0.010
0.015
0.020
Ca/K
(d)
36Ar/40Ar
0.0029
0.0028
0.0027
0.0026
0.0025
0.0024
0.08
0.10
0.12
0.14
0.16
39Ar/40Ar
Age = 9.07±0.60 Ma
Initial 40Ar/36Ar = 297.9±5.8
MSWD= 0.20

Figure 5

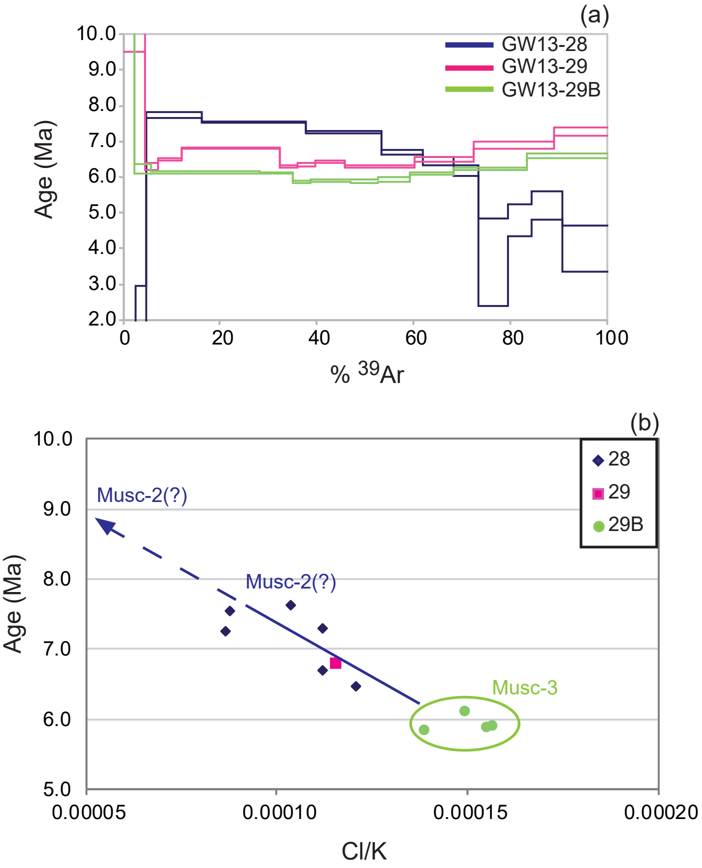
(a)
Age (Ma)
10.0
9.0
8.0
7.0
6.0
5.0
4.0
3.0
2.0
0
20
40
60
80
100
% ^{39}Ar
GW13-28
GW13-29
GW13-29B
(b)
Age (Ma)
10.0
9.0
8.0
7.0
6.0
5.0
0.00005
0.00010
0.00015
0.00020
Cl/K
◆ 28
■ 29
● 29B
Musc-2(?)
Musc-2(?)
Musc-3